Mixing state of refractory black carbon aerosol in the South Asian outflow over the northern Indian Ocean during winter

Sobhan Kumar Kompalli[1], Surendran Nair Suresh Babu[1], Krishnaswamy Krishnamoorthy[2], Sreedharan Krishnakumari Satheesh[2,3], Mukunda M Gogoi[1], Vijayakumar S Nair[1], Jayachandran V[1], Dantong Liu[4],

5   Michael Flynn[4], Hugh Coe[4]

[1]Space Physics Laboratory, Vikram Sarabhai Space Centre, Thiruvananthapuram, India.

[2]Centre for Atmospheric & Oceanic Sciences, Indian Institute of Science, Bengaluru, India.

[3]Divecha Centre for Climate Change, Indian Institute of Science, Bengaluru, India

10   [4]Centre for Atmospheric Science, School of Earth and Environmental Sciences, University of Manchester, Manchester, U.K.

Correspondence to: S. Suresh Babu (sureshsplvssc@gmail.com), Sobhan Kumar Kompalli (sobhanspl@gmail.com)

15

Atmospheric
Chemistry
and Physics
Discussions

Abstract. Regional climatic implications of aerosol black carbon (BC) are well recognized over South Asia, which has a wide variety of anthropogenic sources in a large abundance. Significant uncertainties remain in its quantification due to lack of sufficient information on the microphysical properties (its concentration, size, and mixing state with other aerosol components), which determine the absorption potential of BC. Especially the information on the mixing state of BC is extremely sparse over this region. In this study, first-ever observations of the size distribution and mixing state of individual refractory black carbon (rBC) particles in the south Asian outflow to Southeastern Arabian Sea, northern and equatorial Indian Ocean regions are presented based on measurements using a single particle soot photometer (SP2) aboard the ship cruise of the Integrated Campaign for Aerosols, gases, and Radiation Budget (ICARB-2018) during winter-2018 (16 January to 13 February). The results revealed significant spatial heterogeneity of BC characteristics. The highest rBC mass concentrations (~938 ± 293 ng m^{-3}) with the highest relative coating thickness (RCT; the ratio of BC core to its coating diameters) of ~2.16 ± 0.19 are found over the Southeast Arabian Sea (SEAS) region, which is in the proximity of the continental outflow. As we move to farther oceanic regions, though the mass concentrations decreased by nearly half (~546 ± 80 ng m^{-3}), BC still remained thickly coated (RCT ~ 2.05 ± 0.07). The air over the remote equatorial Indian Ocean, which received considerable marine air masses compared to the other regions, showed the lowest rBC mass concentrations (~206 ± 114 ng m^{-3}), with a moderately thick coating (RCT ~1.73 ± 0.16). Even over oceanic regions far from the landmass, regions that received the outflow from the more industrialized east coast/the Bay of Bengal had thicker coating (~104 nm) than regions that received outflow from the west coast/peninsular India (~86 nm). Although different regions of the ocean depicted contrasting concentrations and mixing state parameters due to varying extent and nature of the continental outflow as well as the atmospheric lifetime of air masses, the modal parameters of rBC mass-size distributions were similar over all the regions. The observed mono-modal distribution with mean mass median diameters (MMD) in the range of 0.19-0.20 µm suggested mixed sources of BC. The mean fraction of BC containing particles (F$_{BC}$) varied in the range 0.20-0.28 (suggesting significant amounts of non-BC particles), whereas the bulk mixing ratio of coating mass to rBC mass was highest (8.77 ± 2.77) over the outflow regions compared to the remote ocean (4.29 ± 1.54) highlighting the role of outflow in providing condensable material for coating on rBC. These parameters, along with the information on the size-resolved mixing state of BC cores, throw light on the role of sources and secondary processing of their complex mixtures for coating on BC under highly polluted conditions. Examination of the non-refractory sub-micrometre aerosol chemical composition obtained using the aerosol chemical speciation monitor (ACSM) suggested that the overall aerosol system was sulfate dominated over the far-oceanic regions. In contrast, organics were equally prominent adjacent to the coastal landmass. Association between the BC mixing state and aerosol chemical composition suggested that sulfate was the probable dominant coating material on rBC cores.

1. Introduction

Black carbon (BC) is the dominant light-absorbing atmospheric aerosol species that perturbs regional and global radiation balance through the positive radiative forcing arising out of its strong absorption of solar radiation and its ability to reduce cloud albedo (Menon et al., 2002; Ramanathan and Carmichael, 2008; IPCC 2013; Bond et al., 2013; Huang et al., 2016).

5 Produced by the incomplete (low-temperature) combustion of hydrocarbon fuels, BC has a global direct radiative forcing of + 0.71 W m^{-2} (+0.08 to +1.26 W m^{-2}), of which fossil and biofuel emissions contribute +0.51 W m^{-2}, and the rest is from biomass burning (Bond et al., 2013). Such large forcing due to BC is reported to be capable of causing significant perturbations to atmospheric circulation, cloud dynamics, rainfall pattern, static stability, and convective activity over regional scales, especially over the Indian region (Menon et al., 2002; Ramanathan et al., 2005; Meehl et al., 2008; Bollasina et al., 2008;

10 Lawrence and Lelieveld 2010; Babu et al., 2011; D'Errico et al., 2015; Boos and Storelvmo, 2016). While fresh BC is fractal-like, hydrophobic, and externally mixed, atmospheric aging results in internally mixed BC with hydrophilic compounds (e.g., organic acids and ammonium sulfate) and altered mixing state, size, and morphology. Also, the aging process leads to enhanced absorption potential of BC (Schnaiter et al., 2005; Shiraiwa et al., 2010; Cappa et al., 2012, 2019; Zhang et al., 2015; Peng et al., 2016; Ueda et al., 2016). The mixing state of BC is a vital parameter that determines its optical and radiative properties

15 (Moffet and Prather 2009; Liu et al., 2017), and is a critical input for the models used to estimate BC direct radiative forcing (Bond et al., 2013). Further, the coating of other soluble species on BC modifies its hygroscopicity and cloud condensation nuclei (CCN) activity (McMeeking et al., 2011; Liu et al., 2013; Laborde et al., 2013), and therefore, the mixing state alters BC-induced cloud changes and indirect radiative effects. Thus, the characterization of BC size and its mixing state is critical to reducing the uncertainties in its direct and indirect radiative effects (Jacobson 2001; Bond et al., 2013).

20 The sources of BC are highly heterogeneous. It has a long atmospheric lifetime. Consequently, the nature and extent of coating on BC vary in space and time, and as such, BC in a polluted environment ages faster than in a relatively clean environment (e.g., Peng et al., 2016; Liu et al., 2010, 2019; Cappa et al., 2019). This calls for region-specific characterization of the spatio-temporal variability of the BC mixing state. This is particularly important over the South Asian region (with rapidly increasing anthropogenic activities and enhanced emissions from a variety of sources) and its outflow into the adjoining oceans (Lawrence

25 and Lelieveld 2010; Babu et al., 2013; IPCC 2013). Aerosol BC over this region has a wide variety of sources (industrial and vehicular emissions, biomass, crop residue, and residential fuel burning) and is co-emitted with a broad spectrum of gaseous compounds which form secondary aerosol species such as sulfates, nitrates, phosphates, and secondary organic aerosols (SOA) (Gustafsson et al., 2009; Pandey et al., 2014) leading to complex mixing states of BC during its atmospheric aging. The absorption potential of the resultant mixed-phase particles would be quite different from those of nascent BC (Lawrence and

30 Lelieveld 2010; Srivastava and Ramachandran, 2013; Srinivas and Sarin 2014; Moorthy et al., 2016). When air masses from such complex source regions are transported to remote regions devoid of any sources of BC, the aging becomes important, and the abundance of distinct species with varying lifetimes in the atmosphere differs significantly. Therefore, the characterization of aerosol and trace species properties gained much attention over the years. Lawrence and Lelieveld (2010) have highlighted many field experiments that attempted to assess the impact of continental outflow of anthropogenic emissions from South Asia

35 to the surrounding oceanic regions and its climate implications. Some of the big field campaigns such as the Indian Ocean Experiment (INDOEX) during 1998-1999 (Ramanathan et al., 2001), the Integrated Campaign for Aerosols, gases, and Radiation Budget (ICARB) during March-May 2006 (phase-1); December-January 2008-2009 (phase-2) (Moorthy et al., 2008; Babu et al., 2012; Kompalli et al., 2013) have provided a wealth of information on the physical, chemical and optical characteristics of the South Asian outflow aerosols and their interaction with the regional climate in different parts of the

40 northern Indian Ocean during different seasons.

However, the information on BC microphysical properties (especially its size distribution, mixing state, and extent of coating) over the northern Indian Ocean remained elusive primarily due to lack of instruments for near-real-time measurements to

estimate BC size and coating on it (Kompalli et al., 2020a). A combination of analytical instruments [such as the single particle soot photometer (SP2) based on laser-induced incandescence technique for the measurements of microphysical properties of refractory BC (rBC) at single particle level (Moteki and Kondo, 2007; Schwarz et al., 2008, 2013; Laborde et al., 2012; Liu et al., 2014), and mass spectroscopy-based aerosol chemical composition measurements (Liu et al., 2014; Gong et al., 2016) such

5   as the aerosol mass spectrometer (AMS), or the aerosol chemical speciation monitor (ACSM) (Ng et al., 2011) that provide near real-time information on the possible coating substances] provides a way to address this issue (Kompalli et al., 2020a and references therein).

In this study, we report such measurements of BC microphysical properties over the Southeastern Arabian Sea, the northern and equatorial Indian Ocean regions, made for the first time. The observations were carried out as a part of the third phase of

10   the Integrated Campaign for Aerosols, gases, and Radiation Budget (ICARB) campaign during the winter season when the above mentioned oceanic regions are strongly impacted by the South Asian outflow aided by the favorable synoptic winds (Lawrence and Lelieveld 2010; Nair et al., 2020). The weak winds and absence of strong precipitation during this season are conducive for longer atmospheric lifetimes and support inter-hemispheric transport of the pollutants. The main aims our measurements included: (i) characterization of the spatio-temporal variation of BC size distributions over the northern Indian

15   Ocean, (ii) the extent of BC transport from distinct source regions and changes to its mixing state during the transport to the ocean, and (iii) the degree of coating on BC and the nature of potential coating species by using concurrent chemical composition measurements during the South Asian outflow. The results of the campaign are presented, and implications are discussed here.

2.   Experimental measurements

20   **2.1 Campaign details and meteorology**

Phase-3 of the 'Integrated Campaign for Aerosols, gases, and Radiation Budget' ship cruise-based experiment (referred to as the ICARB -2018 hereafter) was carried out during the winter period (16 January - 13 February 2018) along the track shown by the solid black line in Fig. 1, covering different parts of the Southeastern Arabian Sea (SEAS), the northern Indian Ocean (NIO), and the equatorial Indian Ocean (EIO), as highlighted by the different boxes about the track. More details about the

25   experiment and sampling conditions are available in earlier publications (Gogoi et al.,2019; Nair et al., 2020; Kompalli et al., 2020b). Briefly, the measurements were made from the specially configured aerosol laboratory on the top deck of the ship, ~15 meters above the sea level, and the instruments sampled air from a community aerosol inlet set up with an upper size cut-off at 10 µm at a flow rate of 16.67 liters per minute (LPM). Membrane-based dryers were installed in the sampling lines to remove the excess moisture (to limit the sampling RH to < 40%). Proper care was taken to avoid the contamination from ship

30   emission by aligning the bow of the ship against the wind direction, and any spurious data were removed during post-processing (as has been done in earlier such campaigns, Moorthy et al., 2008).
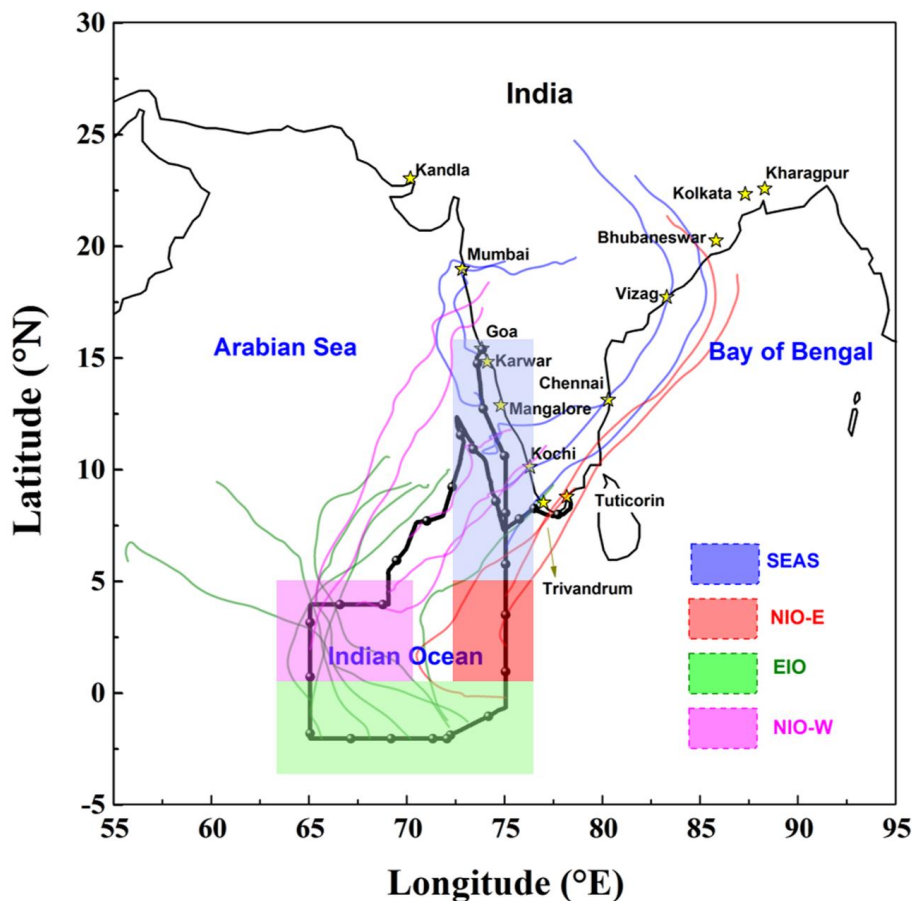
Figure 1. Cruise track of the ICARB-2018 over the northern Indian Ocean from 16 January 2018 to 13 February 2018; the different classified sub-regions are highlighted with shaded portions, and major industrial cities and ports along with the coastline are marked with a star symbol; HYSPLIT five-day isentropic airmass back trajectories arriving at 100 m amsl (dashed lines) above the ship location at 5:30 UTC on each day for different sub-regions are shown in different colors. The filled circles on the track indicate the daily mean position of the ship. SEAS: Southeast Arabian Sea; NIO-E: Northern Indian Ocean-East; EIO: Equatorial Indian Ocean; NIO-W: Northern Indian Ocean-West; Southern Arabian Sea: SAS, this region was affected by rain and weather system. The data from the SAS is not included in the overall analysis.

South Asian region is known for its seasonally contrasting synoptic meteorology associated with the Asian monsoon and north-south excursion of the inter-tropical convergence zone (ITCZ) and monsoonal circulations (Das 1986; Asnani 1993). During the winter (December to February), calm north-easterly winds prevail over the Indian landmass, facilitating extensive transport of continental air mass to the surrounding ocean. The synoptic conditions during the campaign period were quite similar to the climatological pattern, as revealed by Fig. S1 (panel a) in the Supplement, which shows the prevailing synoptic mean wind vectors at 925 hPa derived from ERA-Interim wind data from ECMWF (European Center for Medium range Weather Forecasting; https://apps.ecmwf.int/datasets/data/interim-full-daily/levtype=sfc/) data. The spatial distribution of fire counts over the continental landmass lying upwind of the campaign area, as derived from the Moderate Resolution Imaging Spectroradiometer (MODIS) fire radiative power (MODIS Thermal Anomalies / Fire locations, Collection 6 product obtained

from https://earthdata.nasa.gov/firms) for the period 10 January to 14 February 2018, is shown Fig. S1b. It reveals a significant number of fire events in the upwind regions. Monthly mean tropospheric NO_2 column abundances obtained from TROPOspheric Monitoring Instrument (TROPOMI) (http://www.temis.nl/airpollution/no2col/no2regio_tropomi.php) data, shown in the bottom panels of the same figure (for January 2018 (Fig. S1c) and February 2018 (Fig. S1d)), show significant

5   emissions over the continental areas upwind, a part of which would be transported to the oceanic regions during the ICARB-2018. Earlier, based on the observations using the optical attenuation technique (aethalometer) over the upwind locations (Kharagpur, Bhubaneswar, Vizag, Trivandrum), Kompalli et al. (2013, 2014) have reported that the highest oBC (Optically measured BC) mass concentrations throughout the year are seen during the winter period (mean values ranging from~5389±1245 ng m^{-3} over Trivandrum to 11691 ± 4457 ng m^{-3} over Kharagpur) which highlighted the source strength

10   during this season. Also, the east coast of India is more industrialized compared to the west coast/peninsular India (Fig.S1 c&d; Moorthy et al., 2005; Kompalli et al., 2013).

Air mass back trajectories derived using the Hybrid Single-Particle Lagrangian Integrated Trajectory (HYSPLIT) (https://www.arl.noaa.gov/hysplit/ready/) and shown in Fig. 1, highlight the potential long-range transport of the continental emissions to different oceanic regions covered during the campaign. Accordingly, the cruise region is divided into five distinct

15   sub-regions: (i) Southeastern Arabian Sea (SEAS), which encountered direct outflow from the strong source regions in the western coastal and peninsular India region (shown with blue color box and air mass trajectories); (ii) Northern Indian Ocean-East (NIO-E) (eastern leg of the cruise covering the NIO region), that experienced air mass from the east coast of India and the Bay of Bengal regions (red color); (iii) Equatorial Indian Ocean (EIO), where mostly marine air masses originated/confined within the north-eastern Arabian Sea, and without any direct influence of continental outflow (green color); (iv) Northern

20   Indian Ocean-West (NIO-W), which experiences outflow mainly from western coastal regions of Peninsular India after considerable transit over the Sea (magenta color); and (v) Southern Arabian Sea (SAS), the unshaded region of the track, where widespread rainfall associated with the passage of a large scale meteorological system was encountered. We have not included the data collected over the SAS region in the overall analysis of the present study, and a brief discussion about it is provided in the Supplement. During the rest of the cruise period, calm winds (< 5 m s^{-1}) and clear sky conditions prevailed with no

25   significant variation in air temperature (mean ~ 28 ± 0.8 °C) and relative humidity (mean ~73 ± 5%) conditions. Table-1 gives the details of the regional mean (Avg.), maximum (Max.) and minimum (Min.) values of meteorological variables (air temperature (AT), relative humidity (RH), wind speed (WS), wind direction (WD), total accumulated rainfall (RF) amount) for different regions covered during the ICARB-2018.

Table-1. Regional values of meteorological parameters observed during the cruise period.

Region	AT (ºC)			RH (%)			WS (m s^{-1})			WD	RF
	Avg.	Max.	Min.	Avg.	Max.	Min.	Avg.	Max.	Min.	(º)	(mm)
SEAS	27.6	29.3	26.8	76.2	86.3	65.9	2.7	5.5	0.3	NE	0
NIO-E	28.0	28.7	27.0	69.0	76.5	60.1	3.1	4.8	2.0	NE	0
EIO	28.0	29.1	26.9	72.2	79.4	65.5	4.7	8.8	2.3	NW	0
NIO-W	28.4	28.9	27.7	72.7	78.5	66.1	4.2	6.2	1.7	NW	7.1
SAS	28.2	30.0	27.4	73.9	81.9	61.1	2.8	5.7	0.1	N	50.5

30

2.2 Measurements

Of the several measurements made aboard, the measurements of the BC single particle microphysical properties were carried out using a single-particle soot photometer (SP2) (Model: SP2-D; Droplet Measurement Technologies, Boulder, USA), which was operated at a flow rate of 0.08 liters min^{-1}. The SP2 employs a 1064 nm Nd:YAG intracavity laser, and by using a laser-

Atmospheric
Chemistry
and Physics
Discussions
EGU
Open Access

induced incandescence technique, it characterizes the physical properties of refractory BC (rBC) at the individual particle level (Moteki and Kondo, 2007; Schwarz et al., 2008, 2013; Laborde et al., 2012; Liu et al., 2014; Shiraiwa 2007; Kompalli et al., 2020a). It provides information about mass and number concentrations and size distributions of rBC. The amplitude of the incandescence signal is proportional to the rBC mass present in the BC containing particles, and the mass equivalent diameter

5   (the diameter of a sphere containing the same mass of rBC as measured), or BC core diameter (D_c), is obtained from the measured rBC mass by assuming a density, $\rho \sim 1.8$ g cm^{-3} for atmospheric BC (Bond and Bergstrom, 2006; Moteki and Kondo, 2007, 2010; McMeeking et al., 2011). Further, the amplitude of the scattering signal provides information about the scattering cross-section of the particles, which is used to determine the optical sizing of the particles. In the case of BC containing particles, the scattering signal gets distorted as it passes through the laser beam because of the intense thermal heating of the

10   particle and evaporation of the coating. Thus, the scattering signal of the BC particle is reconstructed using a leading-edge only (LEO) fitting technique, as described in earlier publications (Gao et al., 2007; Liu et al., 2010, 2014, 2017), and this scattering cross-section is matched with the modeled values in a Mie-lookup table to derive the optical diameter of a BC particle or the coated BC size (D_p). These two diameters (D_p and D_c) are used to infer the coating thickness. Before the experiment, the SP2 was calibrated by using Aquadag® black carbon particle standards (Aqueous Deflocculated Acheson Graphite, manufactured

15   by Acheson Inc., USA), and a correction factor of 0.75 is applied to address the difference between Aquadag® standards and ambient BC (e.g., Moteki and Kondo 2010; Laborde et al., 2012). A detailed description of the instrument, data interpretation procedures, uncertainties, and caveats involved can be found elsewhere (Liu et al., 2010,2014; McMeeking et al., 2010; Sedlacek III et al., 2012, 2018; Kompalli et al., 2020a).

Supplementing the above, we have used the information on the mass concentration of non-refractory PM1.0 aerosols

20   (organics, sulfate, ammonium, nitrate, and chloride) from a collocated aerosol chemical speciation monitor (ACSM; Model: 140; Aerodyne, USA). The objective here is to identify the possible coating material on rBC particles. The ACSM uses quadrupole mass spectrometry, where the particles having aerodynamic vacuum diameters in the range ~40-1000 nm are flash vaporized by the thermal capture vaporizer operating at 525 °C. Subsequently, these vapors are ionized via 70 eV electron impact ionization and detected with a quadrupole mass spectrometer. The data is processed as per the prescribed methodology

25   (Ng et al., 2011; Middlebrook et al., 2012; Kompalli et al., 2020a).

2.3 Analysis

The extent of coating on rBC particles is quantified in terms of the bulk relative coating thickness (RCT) defined as D_p/D_c, where D_p and D_c are coated and core BC particle diameters, respectively. It is estimated by dividing the total volume of coated BC with that of rBC cores in a given time window (5 minutes in our case) following Liu et al. (2014, 2019):

30

$$\frac{D_p}{D_c} = \sqrt[3]{\frac{\sum_i D_{p,i}^3}{\sum_i D_{c,i}^3}} \qquad (1)$$

where $D_{p,i}$, and $D_{c,i}$ are the diameters of coated and core rBC respectively for each single particle i. In addition to RCT, we have used bulk volume-weighted absolute coating thickness (ACT, in nm), defined as $(D_p-D_c)/2$ (both D_p and D_c used here are volume averaged diameters) based on the assumption of a concentric core-shell morphology, as another diagnostic of the coating on the population of rBC particles (Gong et al., 2016; Cheng et al., 2018; Brooks et al., 2019). More details about the

35   parameters bulk RCT and ACT, the methodology used here, and uncertainties associated were described elsewhere (Liu et al., 2017, 2019; Sedlacek III et al., 2018; Brooks et al., 2019; Kompalli et al., 2020a).

The means of the mass median diameter (MMD) and number median diameters (NMD) were determined from the size distributions of BC cores for each time window by least-squares fitting to an analytical monomodal log-normal distribution (Liu et al., 2010, 2014; Kompalli et al., 2020a) of the following form:

40

$$\frac{dX}{d \ln D_q} = \sum \frac{X_0}{\sqrt{2\pi} \ln \sigma_m} exp\left[-\frac{(\ln D_q - \ln D_m)^2}{2 \ln \sigma_m}\right] \qquad (2)$$

Atmospheric
Chemistry
and Physics
Discussions
Open Access
EGU

Here X_0 corresponds to mass/number concentration of the mode, D_m is the mass/number median diameter, D_q is particle diameter, dX is mass/number concentrations in an infinitesimal diameter interval $dlnD_q$, and σ_m is the geometric standard deviation (of the median diameter).

Using the bulk RCT and MMD of the BC cores, the volume-weighted coated BC size ($D_{p,v}$) is calculated as below, to

5   indicate the mean coated BC size:

$$D_{p,v} = \frac{D_p}{D_c} \times MMD \tag{3}$$

Since the ratio of the mass of non-absorbing coating material to the rBC core is an important parameter in determining the degree of absorption enhancement of BC, we quantified their mixing in terms of the bulk mixing ratio of coating mass over rBC mass ($M_{R,bulk}$) derived by assuming densities for the bulk coating ($\rho_{coating}$ ~1.7 g cm^{-3}) and rBC core ($\rho_{rBCcore}$ ~1.8 g cm^{-3})

10   (Liu et al., 2019) as below:

$$M_{R,bulk} = \left(\left(\frac{D_p}{D_c}\right)^3 - 1\right) \times \frac{\rho_{coating}}{\rho_{rBCcore}} \tag{4}$$

To explore the distribution of BC core-coatings, a parameter of scattering enhancement (E_{sca}) for each single particle is determined using the expression (Liu et al., 2014, 2019):

$$E_{sca} = \frac{S_{measured,coatedBC}}{S_{calculated,uncoatedBC}} \tag{5}$$

15   where the term in the numerator is the scattered light intensity of the coated rBC particle measured by the scattering detector of the SP2 and reconstructed using the LEO technique, while the denominator is the scattering intensity of the uncoated BC calculated using Mie single particle scattering solutions, assuming sphericity (Liu et al., 2014, 2019; Taylor et al., 2014; Brooks et al., 2019). For this purpose, the measured rBC mass and a refractive index of BC ~2.26 ± 1.26i (Moteki et al., 2010) at the SP2 laser wavelength, ~1064 nm, were used. For an uncoated rBC particle, E_{sca} is equal to 1, and E_{sca} increases with an increased

20   coating at a given core size. Combined with rBC core diameters and coating parameters, E_{sca} is helpful in identifying the nature of sources.

3. Results and discussion

3.1 Spatial distribution of rBC mass/number concentrations and size distributions

25   The spatial variations of the number and mass concentrations of refractory BC core particles during the cruise, along with the statistics over different regions depicted using the box-and-whisker plots, are shown in Fig.2.
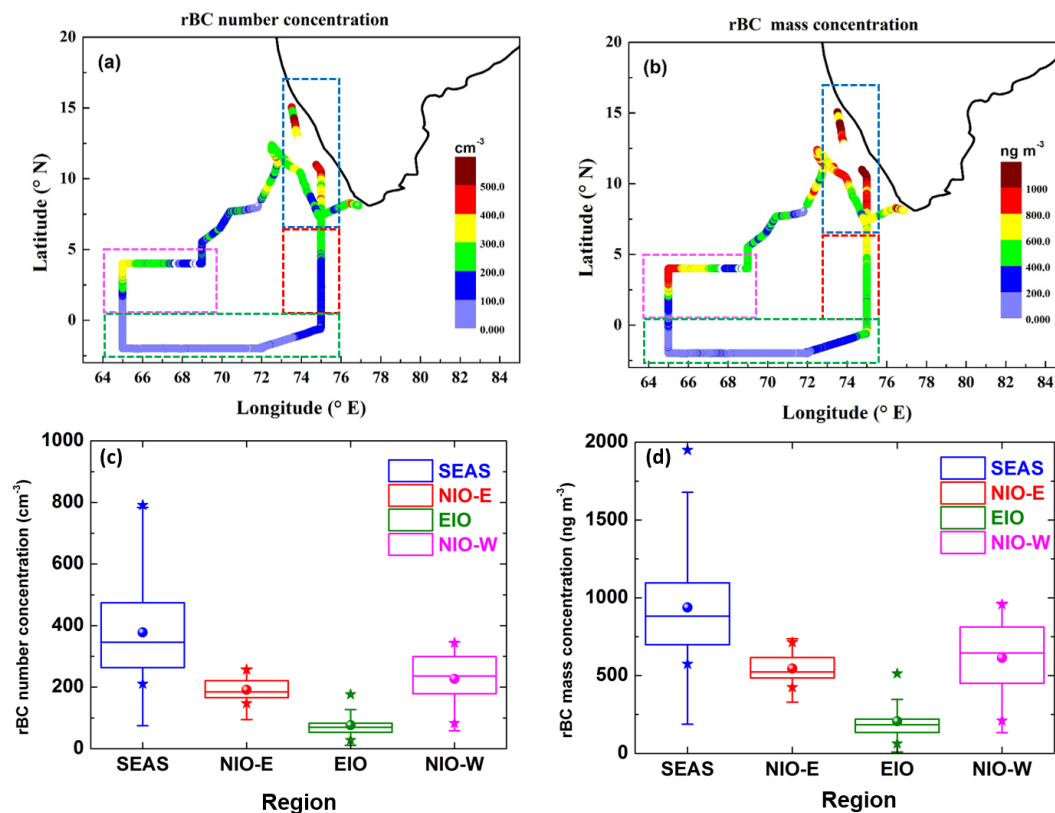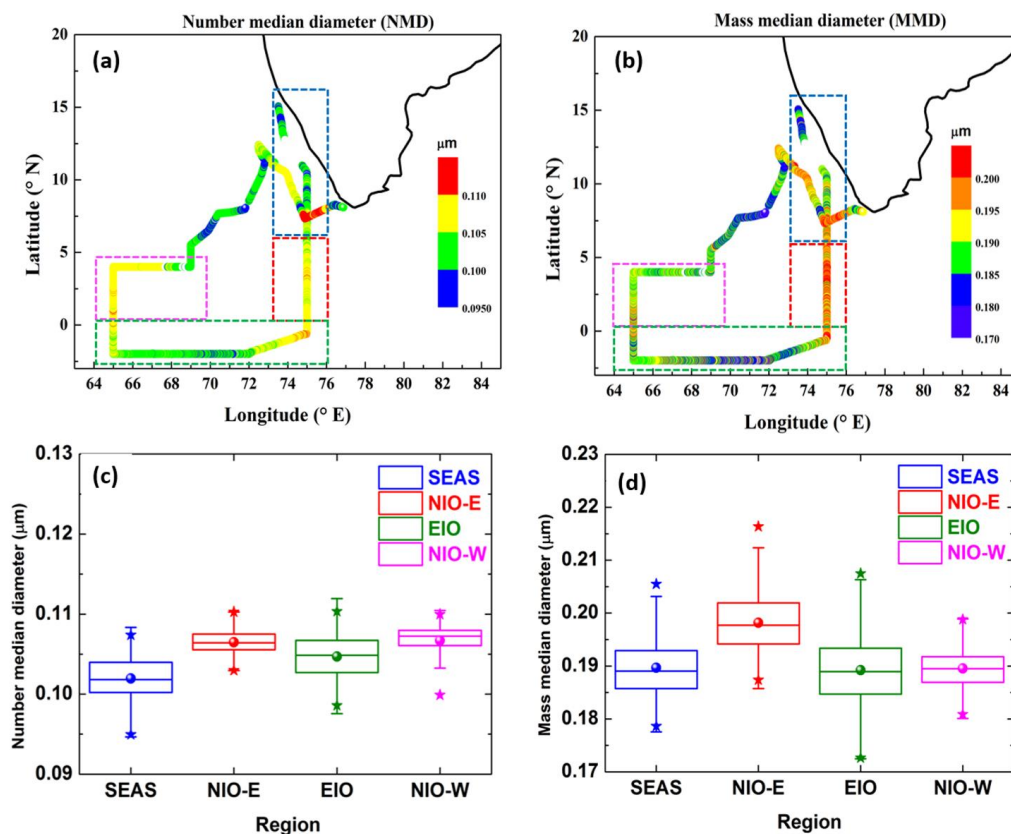
Figure 2. **Spatial distribution and the box-and-whisker plots of refractory BC (rBC) number (a & c) and mass concentrations (b& d). The color scale in the spatial map (upper panels) indicates the magnitude of the property. Rectangles with dashed borders highlight different sub-regions. The box-and-whisker plots (bottom panels) illustrate the mean (sphere), median (the horizontal bar in the box), 25th and 75th percentile (the lower and upper lines of the box), 5th and 95th percentile (end of error bars), and maximum and minimum values for the regions (as solid stars).**

The highest values and variabilities in the rBC mass (mean ~938 ± 293 ng m^{-3}) and number (~378 ± 137 cm^{-3}) concentrations are noticed over the SEAS region, which is in the proximity of the source regions/outflow from the western coast and peninsular India, where industrialized cities and major ports are located (Fig.1 & Fig.S1). The strength of advected aerosols was also noticed in other onboard measurements when the cruise was parallel to the western coast and off Trivandrum (8.5 °N, 77 °E) where the oBC values (from aethalometer) were in the range ~2000-2500 ng m^{-3}. The concentrations decreased gradually by half as the ship headed towards the NIO-E (eastern leg of the NIO), where it received outflow mostly from the east coast/ the Bay of Bengal regions. The lowest concentrations (which were 4-5 folds lower than the values seen over the SEAS) are observed over the remote EIO region. Such extremely low concentrations (<200 ng m^{-3}) highlighted the cleaner nature of this region, which encountered mostly oceanic air masses. The concentrations increased again (almost by 3-folds compared to the values seen over the EIO region) as the ship traversed to the NIO-W (western leg of the NIO) region, which experienced continental outflow air masses from the west coast/peninsular India; similar to the SEAS, but farther from the coast and SEAS region. Thus, the concentrations in the NIO-W were lower than those seen in the SEAS and comparable to those seen in its eastern counterpart (NIO-E). This also indicated varying amounts of BC in the outflow from different parts of the peninsula, apparently due to different source strengths and transit times involved. A similar spatial variability pattern was also reported for other aerosol parameters during the present campaign (Gogoi et al., 2019; Nair et al., 2020; Kompalli et al., 2020b).

The size distributions of rBC are influenced by the source, sinks, and transformation processes taking place during advection and are known to be important in assessing the light absorption characteristics (Reddington et al., 2013). In general, urban regions dominated by fresh fossil fuel emissions consist of smaller BC cores (MMD < 0.16 µm). In contrast, the areas with dominant solid-fuel sources (biomass, biofuel, coal-burning) consist of BC particles with larger mass median diameters (>

5   0.22 µm). On the other hand, aged BC particles in continental outflow regions comprised BC particles with MMD in the range ~0.18-0.20 µm (McMeeking et al., 2010; Liu et al., 2010, 2014; Kondo et al., 2011; Cappa et al., 2012; Sahu et al., 2012; Laborde et al., 2013; Reddington et al., 2013; Gong et al., 2016; Raatikainen et al., 2017; Brooks et al., 2019; Kompalli et al., 2020a). The spatial distribution of mass median diameter and number median diameters during the ICARB-2018 shown in Fig. 3 was interpreted based on this backdrop. The observed narrow range of mean NMD (0.10-0.11 µm) and MMD (0.19-

10   0.20 µm) over the entire region (Fig. 3c and 3d) reveals that the prevailing BC over the entire study region has a mixed-source origin and the particles are aged during the long advection leading to transformation processes (such as collapsing of the BC cores). Notably, the NIO-E region depicted slightly larger mean MMD (~0.20 µm) due to frequent larger values (35 % of the measurements showed MMD> 0.20 µm) compared to all the other regions (Fig. 3d). This is a result of either of two possibilities: (i) Self-coagulation of rBC cores due to enhanced atmospheric aging, which increases the rBC core diameters (at

15   the same time, sedimentation of larger particles resulting in a large reduction in number concentration and mass concentration); (ii) The second and less likely possibility of a sizeable contribution (though not dominant) from solid fuel sources (biomass/crop residue/coal burning) in the upwind regions to the observed BC concentrations which were transported by the air masses traversing through the eastern coast of India and the Bay of Bengal (Brooks et al., 2019; Kompalli et al., 2020a). Interestingly, the EIO region showed the largest variability with a non-negligible contribution (~8 %) from smaller BC cores

20   (MMD < 0.18 µm). Over NIO-W, the MMD values remained between 0.18-0.20 µm suggesting advection of BC originating from mixed sources over peninsular India/west coast.

Atmospheric
Chemistry
and Physics
Discussions

Figure 3. Spatial distribution and the box-and-whisker plots of number median diameter (NMD) (a & c), and mass median diameter (MMD) (b & d) of rBC core size distributions during the ICARB-2018. The color scale in the spatial map (upper panels) indicates the magnitude of the parameter. Rectangles with dashed borders highlight different sub-regions. The box-and-whisker plots (bottom panels) illustrate the mean (sphere), median (the horizontal bar in the box), 25th and 75th percentile (the lower and upper lines of the box), 5th and 95th percentile (end of error bars), and maximum and minimum values for the regions (as solid stars).

The spatial distribution of NMD also showed a similar picture to that of MMD over all the regions. We have compared the MMD values of rBC observed in our campaign, with the values reported from selected locations with distinct dominant sources in different environments in Table-2.

Table-2: A comparison of rBC mass median diameters/mode of mass size distributions (MSD) reported from selected locations with distinct sources in different environments.

| S.No.	Location	Type of location	MSD mode/ MMD (μm)	Reference
1.	Southeastern Arabian Sea	Continental outflow/mixed sources	0.18-0.20 (mean~0.19± 0.01)	Present study
2.	Northern Indian Ocean	Continental outflow/mixed sources	0.19-0.21	Present study
3.	Equatorial Indian Ocean	Outflow impacted remote marine/mixed sources	0.18 -0.21 (mean~0.19 ± 0.01)	Present study

4.	Bhubaneswar, India	Urban/fresh urban emissions	0.17 ± 0.01	Kompalli et al., (2020a)
		Urban/continental outflow, aged BC	0.18-0.19	
		Urban/with high solid fuel emissions	0.22 ± 0.01	
5.	Indo-Gangetic Plain (aircraft experiment)	Urban polluted/mixed sources	0.18-0.21	Brooks et al. (2019)
6.	Beijing, China	Urban/mixed sources	0.19-0.21	Liu et al. (2019)
7.	Gual Pahari, India	Urban polluted/ fresh biofuel, crop residue	0.22 ± 0.01	Raatikainen et al. (2017)
8.	Shanghai, China	Urban/pollution episode with high biomass burning	0.23	Gong et al. (2016)
9.	Suzu, Japan	Urban/east Asian outflow site	0.200	Ueda et al. (2016)
10.	Jungfraujoch, Switzerland	High-altitude remote background / biomass burning, aged BC	0.22-0.24	Liu et al. (2010)
11.	Mukteshwar, the Himalayas, India	High-altitude/biofuel, crop residue outflow	0.21 ± 0.02	Raatikainen et al. (2017)
12.	Regional average over Europe	Near source to high-altitudes	0.17-0.21 (a) continental pollution (0.18-0.21); (b) urban outflow (0.17 ± 0.01)	McMeeking et al. (2010)
13.	Canadian oil sand mining, Canada	Urban/fresh urban emissions	0.135-0.145	Cheng et al. (2018)
14.	London, England	Urban/traffic emissions Wood burning	0.119-0.124 0.170	Liu et al. (2014)

As evident from Table-2, the MMD values during ICARB-2018 mostly fall in the category of BC from the continental outflow and originated from mixed sources (McMeeking et al., 2010, 2011; Ueda et al., 2016; Cheng et al., 2018). Recently, Kompalli et al. (2020a) had also reported mean MMD values of 0.18-0.19 μm over Bhubaneswar (located in the east coast of India) during the winter when urban continental outflow with mixed sources from the Indo-Gangetic Plain prevailed. Similarly, Liu et al. (2019) have reported MMD ~0.19-0.21 μm in the urban environment of Beijing with mixed sources. The mean MMD values (Table-2) and mass size distributions over different regions covered in this study (Fig. S2 in the Supplement) revealed that though the peak amplitudes varied in proportion to the magnitude of the BC loading, which decreased with increasing distance from the peninsula, the modal diameters (0.19-0.20 μm) showed little variability, which is also underlined by similar geometric standard deviation values ~1.55-1.59. This is also consistent with the widespread nature of the continental outflow to the northern Indian Ocean (from west to east) and mixed sources for rBC particles in the outflow (McMeeking et al., 2010).

3.2 Spatial variation of the BC aerosol mixing state

3.2.1 The bulk coating parameters: RCT and ACT

The variation of bulk relative coating thickness (RCT) estimated using eq.1, and absolute coating thickness (ACT) describes the physicochemical changes in the characteristics of rBC taking place during atmospheric aging from the outflow to the oceanic regions. The spatial variation of these parameters during the cruise are shown in the top panels of Fig. 4, while the bottom panels show the frequency of occurrence of these parameters over the different oceanic regions. Corresponding median values are also written in the figures.

Atmospheric
Chemistry
and Physics
Discussions

Open Access

EGU
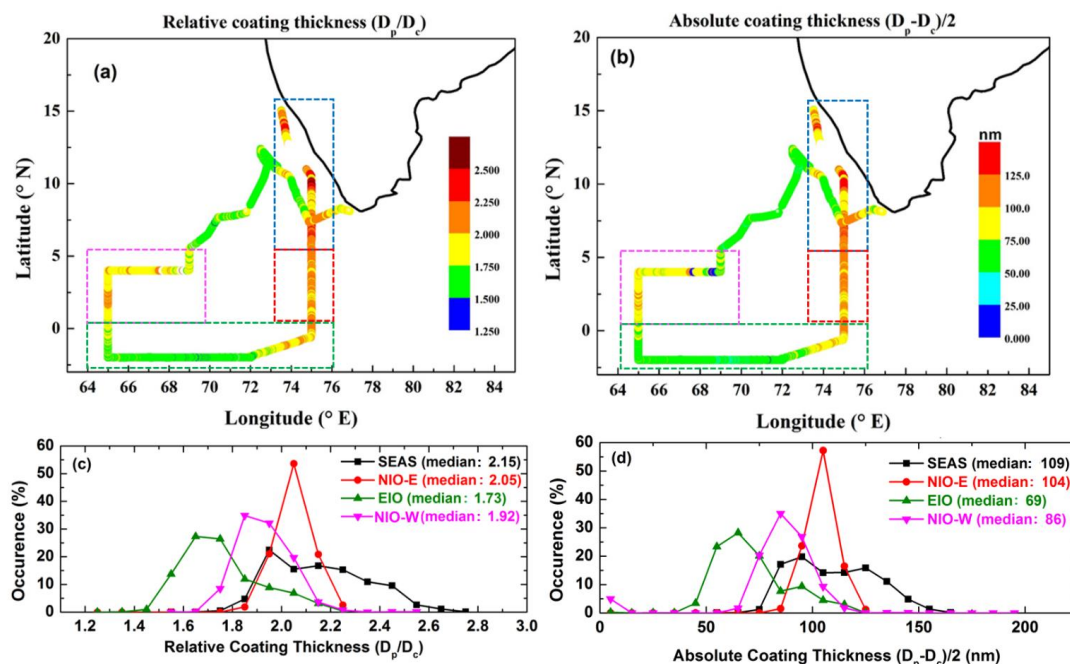
Figure 4. Spatial variation of the bulk (a) relative coating thickness (D$_p$/D$_c$), (b) absolute coating thickness ((D$_p$-D$_c$)/2), (the color scale indicates the magnitude) and (c-d) frequency of occurrence of the bulk RCT and ACT in different oceanic sub-regions (shaded following the criteria in Figure 1). Sub-regional median values are written in the bottom panels.

The median values show a clear spatial variation of the coating thicknesses (both RCT and ACT), being highest over the SEAS (closest to the coast) and lowest over the EIO (farthest from the landmass). This is attributed to the steadily decreasing concentrations of the coating material in the outflow, due to possible dispersion and reactions. The SEAS region, which is in proximity to the coast and immediately impacted by the outflow, displayed a wide range of coating values (Fig.4c & 4d), with the highest overall median values (RCT~ 2.15 and ACT~109 nm). Notably, two peaks of comparable magnitudes (RCT~1.95 and 2.3; ACT ~ 93 and 126 nm) are visible in the frequency distribution over this region (Fig. 4d), highlighting the large variability due to varying amounts of condensable species and rBC aging. Nearly 95% of measurements indicated that rBC particles have an additional coating over its cores to the extent of > 90% of its size. Such high levels of the coating indicate the availability of high concentrations of condensable materials in the outflow as have also been reported by other investigators elsewhere (e.g., Gong et al., 2016; Liu et al., 2019; Brooks et al., 2019). In contrast, over the NIO-E region, only thickly coated BC particles are observed, where the frequency distributions show a narrow/ sharp peak for bulk RCT (median ~2.05) and ACT (median ~104 nm). It highlighted the contrasting nature of the condensable coating material in the Bay of Bengal/east coast outflow channel compared to the west coast/ peninsular India outflow channel. Earlier, Moorthy et al. (2005) showed that the east coast /coastal Bay of Bengal has stronger hotspots of surface aerosols and gases, as well as a higher abundance of submicron aerosols. Such variability in the species concentrations in the outflow channels is responsible for the marked contrast in the coating parameters examined here.

As we move farther to the EIO region, RCT and ACT decreased conspicuously, with median values of 1.73 and 69 nm, respectively, with frequency distributions skewed towards lower values. It may be recollected that the lowest BC loading was also noticed over this region (Fig. 2), which experienced air masses that have spent considerable time in the marine atmosphere. The lower coating thickness here is attributed to dilution of the outflow and preferential scavenging processes during the

advection restricting the concentrations of both the BC particles and condensable material. With aging, BC particles become increasing internally mixed with condensable soluble material, which enhances their removal probability by dry deposition and in-cloud scavenging processes in the atmosphere, including both nucleation scavenging and scavenging by the pre-existing cloud droplets (Miyakawa et al., 2017; Ueda et al., 2018; Zhang et al., 2008). While the larger BC particles are scavenged

5 rather quickly, the smaller, less-aged, and relatively less-coated BC particles (occasionally, even bare soot particles) can persist in the outflow and be transported to the remote marine regions (Ueda et al., 2018). This explains the broad range of MMD (Fig. 3d) and lower RCT values observed over the EIO. Furthermore, in cleaner maritime regions like the equatorial Indian Ocean, the aging of BC occurs slowly due to reduced availability of coating material. It possibly resulted in the observed inferior coatings on rBC over the EIO region. As the impact of continental outflow increases in the NIO-W, the coating on

10 rBC increased once again (median RCT ~1.92 and ACT~86 nm). Interestingly, highly coated BC particles were found less frequently over the NIO-W (with west coast air masses) compared to its eastern counterpart, the NIO-E region, which experienced east coast/Bay of Bengal air masses originating from more industrialized upwind locations, e.g., Moorthy et al., 2005; Kompalli et al., 2013). Thus, a clear contrast in the mixing state parameters is evident which is due to the nature of prevailing distinct air masses (extent of pollution levels) (Moorthy et al., 2008; Peng et al., 2016; Gong et al., 2016), and the

15 difference in their atmospheric transit time over these two regions.

It is known that the BC mixing state depends on various factors, which include the BC size distribution, nature of sources, the concentration of condensable materials that BC encounters during its atmospheric lifetime, and processes such as photochemical aging (Liu et al., 2013; Ueda et al., 2016; Miyakawa et al., 2017; Wang et al., 2018). The values of BC coating parameters (bulk RCT and ACT) seen in the present study that examined outflow characteristics are comparable to the values

20 reported in pollution in-plume air mass regions elsewhere (e.g., Cheng et al., 2019; Brooks et al., 2019). Recently, Kompalli et al. (2020a) have reported seasonal mean bulk relative coating thickness (RCT) in the range ~1.3-1.8 and ACT~ 50-70 nm over Bhubaneswar when the site received polluted outflow from the Indo-Gangetic Plain (IGP). Brookes et al. (2019) have noticed thickly coated BC particles (ACT~50-200 nm) across northern India, especially the IGP and north-east India, during their recent aircraft experiments. It may be noted that direct comparison of present coating parameters with those reported in

25 other studies cannot be made due to different system configurations, the range of volume equivalent diameters covered by the instruments, and different techniques used in the estimation the optical diameters from scattering amplitudes (Gong et al., 2016; Raatikainen et al., 2017; Cheng et al., 2018; Liu et al., 2019). Also, the earlier studies are mostly made in the 'near-field' situation, whereas the present study examined the coating characteristics in a 'far-field' scenario (far away from potential sources, especially NIO and EIO regions). Nevertheless, such high degree of coatings on BC considerably enhances its

30 absorption cross-section, thereby, causes substantial absorption enhancement (by the factors in the range of 1.6-3.4) and affects the radiative forcing (Moffet and Prather 2009; Shiraiwa et al., 2010; Thamban et al.,2017; Liu et al., 2015; Wang et al., 2018). It needs further detailed investigation in future studies.

3.2.2 Coated BC diameter, F_{BC}, and bulk mixing ratio ($M_{R,bulk}$)

The spatial variation of number concentration (in cm^{-3}) of non-BC (i.e., purely scattering) particles detected by the SP2 and

35 the fraction of rBC-containing particles (F_{BC}; the ratio of rBC number concentration to the total number concentration, which is the sum of number concentrations of BC and non-BC scattering particles) are shown in Fig. 5 (a & b). In the bottom panels of the same figure are shown the volume-weighted coated BC size ($D_{p,v}$) (in µm) (Fig. 5c) and bulk mixing ratio of coating mass to rBC mass ($M_{R,bulk}$) (Fig. 5d) calculated using the equations. 3 and 4.
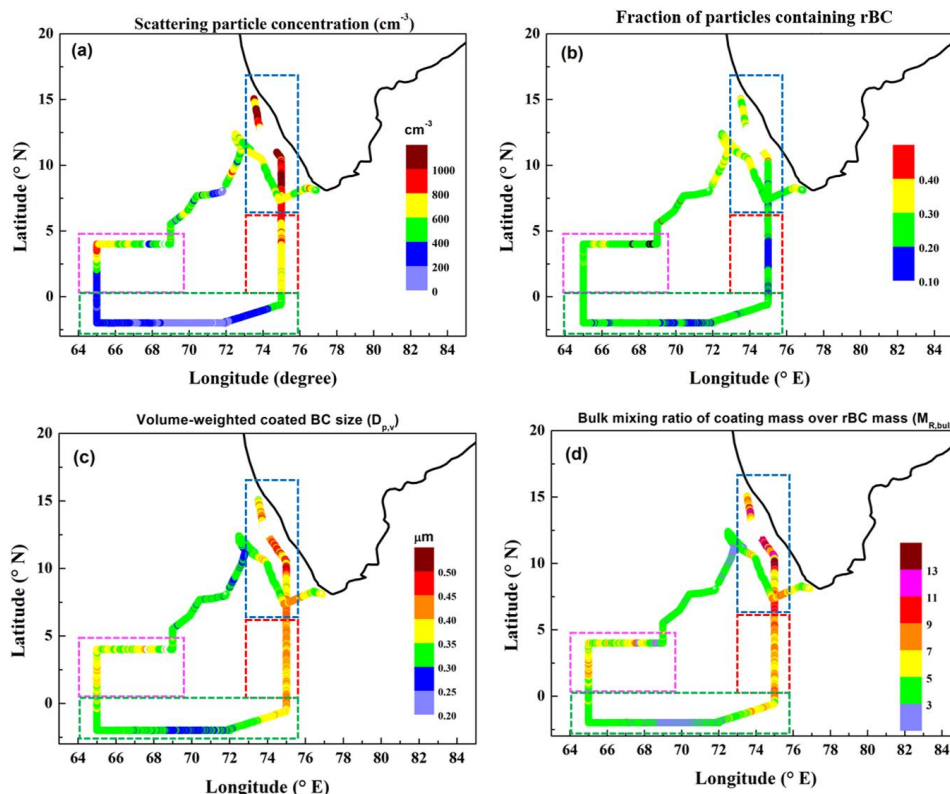
Figure 5. Spatial variation of the (a) scattering (non-BC) particle number concentration (in cm^{-3}), (b) fraction of rBC-containing particles (F$_{BC}$), (c) volume-weighted coated BC size (D$_{p,v}$) (in μm), and (d) bulk mixing ratio of coating mass to rBC mass (M$_{R,bulk}$). Rectangles with dashed borders highlight different sub-regions.

5   The overall spatial variation patterns of scattering particle concentrations and various mixing state parameters are similar to those of the rBC mass and number concentrations seen earlier, with the highest values over the SEAS, decreasing gradually towards the NIO (east and west) to reach the lowest values over the remote EIO. The figure reveals the following:

   (i) The non-BC (scattering) particle concentrations were very high, >1000 cm^{-3}, in the coastal waters (the SEAS), decreasing towards farther oceanic regions and reached values as low as <200 cm^{-3} in the remote EIO in-line with the
10   expected reduction in the influence of the sources (Fig. 5a).

   (ii) The rBC particles constituted about 25% to 35% of the total number concentration over almost the entire oceanic region north of 5 °N. It occasionally decreased to 15 to 20 % over farther oceanic regions. The F$_{BC}$ values showed the largest variability over the SEAS among all the regions (Fig. 5b).

   (iii) Coated rBC particles were larger (D$_{p,v}$ ~0.35-0.50 μm) over coastal waters (SEAS), highlighting a substantial
15   enhancement of the overall rBC particle sizes due to thick coatings on them in the polluted outflow air masses. The values diminished farther away, and the lowest values (<0.30 μm) are seen over the EIO region (Fig. 5c).

   (iv) The bulk mixing ratio of coating mass over rBC mass (M$_{R,bulk}$) revealed high values (4.5-18.3) with large variability over the regions with extensive outflow (SEAS) due to the presence of thickly coated BC particles in these regions. Though M$_{R,bulk}$ values were very low over EIO, occasional high values (> 4.5) are also seen (Fig. 5d).

20   Interestingly, concentrations of scattering (non-BC) particles (Fig. 5a) over the SEAS (mean ~ 973 ± 187 cm^{-3}) and the NIO-E (mean ~747 ± 69 cm^{-3}) are comparable to or higher than the values reported over the IGP outflow site, Bhubaneswar (winter

mean $\sim 950 \pm 464$ cm^{-3}; annual mean $\sim 702 \pm 458$ cm^{-3}) as reported by Kompalli et al. (2020a). This highlighted the strength of the outflow to the oceanic regions. Any increase in non-BC particle abundance impacts the fraction of rBC containing particles. The mean fraction of rBC containing particles (F_{BC}) was in the range 0.20-0.28 over different sub-regions, and the lowest mean values were seen over the NIO-E, which received the east coast/ Bay of Bengal air masses. The F_{BC} values over the northern

5   Indian Ocean are comparable to the values ($F_{BC} \sim 0.24$) reported over the Finnish Arctic, a background site receiving aged air masses (Raatikainen et al., 2015). However, earlier studies over the continental landmass of India have shown much higher number fractions with mean F_{BC} values $\sim 0.51 \pm 0.02$ and 0.50 ± 0.03 over two stations, Gual Pahari (polluted site) and Mukteshwar (regional background site) in northern India (Raatikainen et al., 2017). This was attributed to the strong influence of regional anthropogenic activities on BC loading. Kompalli et al. (2020a) had reported widely varying mean fractions (0.25-

10   0.69 in different seasons) over Bhubaneswar (eastern India). They suggested that the scattering (non-BC) particle population detectable with the SP2 varied seasonally, thereby contributing to observed seasonal F_{BC} variation. In the light of the above, the presence of lower F_{BC} values over the marine regions in this study, which received a strong continental outflow, is not surprising, and along with the observed significant non-BC particles in the detection range of the SP2 (200-400 nm) (along with rBC particles) corroborated the higher coatings on BC.

15   Strong continental outflows (from the polluted regions) are more likely to contain significant amounts of condensable material that can act as a potential coating on rBC (Liu et al., 2014, 2019; Raatikainen et al., 2017). This is reflected in the observed high values of coated BC particle diameters (0.36-0.55 µm) in this study (Fig.5c). The present $D_{p,v}$ values over the northern Indian Ocean region are higher than those recently reported by Brooks et al. (2019) ($\sim$0.25-0.30 µm) over the IGP and eastern India, but comparable to the values reported by Raatikainen et al., (2017) for thickly coated BC particles in polluted

20   outflow environments in northern India highlighting the similarity of the outflow strength (concentrations of the condensable species).

    The impact of the extensive outflow is evident also from the observed very high values of another important mixing state parameter, the bulk mixing ratio of coating mass over rBC mass ($M_{R,bulk} \sim 4.5$-18.3) (Fig. 5d) over the adjacent marine regions, which is due to the presence of thickly coated BC particles. Such high $M_{R,bulk}$ values were reported in the literature

25   from extremely polluted environments and biomass burning source dominant regions (Liu et al., 2017; 2019). The presence of such non-absorbing coated mass on the rBC cores has significant radiative implications. Recently, Liu et al. (2017) have examined the measured and modeled optical properties of BC as a function of mass ratio ($M_{R,bulk}$) under different environments, and found that significant absorption enhancement occurs when the coating mass over rBC mass is larger than 3. They suggested that in such a scenario (i.e., $M_{R,bulk}$ >3), the core-shell model reproduces the measured scattering cross-section.

30   Present high $M_{R,bulk}$ values, which are consistent with the values reported by Liu et al. (2017, 2019), could be due to the combined effects of both emissions (substantial concentrations of coating material originating from distinct sources in the South Asian outflow) and atmospheric processes (considerable aging of the particles before reaching the adjacent oceanic region).

    A summary of rBC physical properties and mixing state parameters in different oceanic regions are presented in

35   Table-3.

Table-3: A summary of regional mean values of rBC physical properties and mixing state parameters during the ICARB-2018. The values after ± are standard deviations.

Parameter	SEAS	NIO-E	EIO	NIO-W
rBC mass concentration (ng m^{-3})	938±293	546 ± 80	206 ± 114	614 ± 211
rBC number concentration (cm^{-3})	378 ± 137	191 ± 32	76 ± 38	227 ± 76
Scattering particle concentration (cm^{-3})	973 ± 187	747 ± 69	262 ± 140	580 ± 156
Mass median diameter (µm)	0.19 ± 0.01	0.20± 0.01	0.19± 0.01	0.19 ± 0.004

|				
Number median diameter (µm)	0.10 ± 0.002	0.11± 0.003	0.11± 0.003	0.107 ± 0.002
Relative coating thickness	2.16 ± 0.19	2.05 ± 0.07	1.76 ± 0.16	1.93 ± 0.10
Absolute coating thickness (nm)	109 ± 20	104 ± 7	72 ± 17	85 ± 21
Fraction of rBC-containing particles (F_{BC})	0.27 ± 0.05	0.20 ± 0.02	0.23 ± 0.03	0.28 ± 0.02
volume-weighted coated BC size ($D_{p,v}$) (µm)	0.41 ± 0.04	0.41 ± 0.01	0.33 ± 0.04	0.37 ± 0.02
Bulk mixing ratio of coating mass over rBC mass ($M_{R,bulk}$)	8.77 ± 2.67	7.24 ± 0.87	4.3 ± 1.52	5.88 ± 1.15

Table-3 highlights the spatial heterogeneity in rBC microphysical properties over the northern Indian ocean. It reveals the contrast in outflow strength with varying extents BC and non-BC species abundance in the west coast/peninsular India, east coast/Bay of Bengal air masses. Table-3 also highlights the diminishing strength of the outflow as seen from the lower concentrations, coatings and associated mixing state parameters over the EIO region.

5 **3.3 BC segregation by size-resolved mixing state**

The above discussions have established that:

(i) The extent of the coating as measured by the coating thickness and the bulk mixing ratio of coating mass over rBC mass, and hence the mixing of BC with condensable species, is highest closer to the coast where the outflow is strong and decreases to farther oceanic regions.

10 (ii) The rBC core diameters, as well as the fractional concentration of rBC to total concentration, remained more or less comparable throughout the oceanic regions surveyed, suggesting an impact of similar sources of mixed origin. However, the coated BC diameters varied according to the magnitude of coating over different regions.

To examine these common sources, the size-resolved BC mixing state is examined from the variation in scattering enhancement (E_{sca}, equation. 5) as a function of BC core diameter (D_c) in Fig.6. The corresponding bulk absolute coating 15 thickness (ACT) values are mapped to the E_{sca} (solid white lines) in the figure. Following the methodology described in the previous publications (Liu et al., 2014, 2019; Brooks et al., 2019), the BC particles are segregated according to the discontinuous distribution in E_{sca}- D_c (dashed black lines in the figure). Four classes of BC particles are described as: (a) small BC with a thin coating, i.e., with BC core diameters < 0.18 µm and ACT < 50 nm; (b) moderately coated BC, with ACT in the range 50–200 nm; (c) thickly coated BC with ACT> 200 nm; and (d) large uncoated BC, with BC core size >0.18 µm and 20 coating thicknesses < 50 nm. In the present study, there is no noteworthy presence of a clear 'smaller sized BC with a thin coating', which is generally attributed to fresh traffic emissions (e.g., Liu et al. (2014) over London; Liu et al. (2019) over Beijing). Brooks et al. (2019) also found smaller contributions from such particles during aircraft observations over northwest and northeast parts India carried out in the dry season. It appears logical, as the particles over the oceanic regions are rather aged, and away from the potential sources, which are mostly located over the continental landmass, upwind.

Atmospheric
Chemistry
and Physics
Discussions
Open Access
EGU
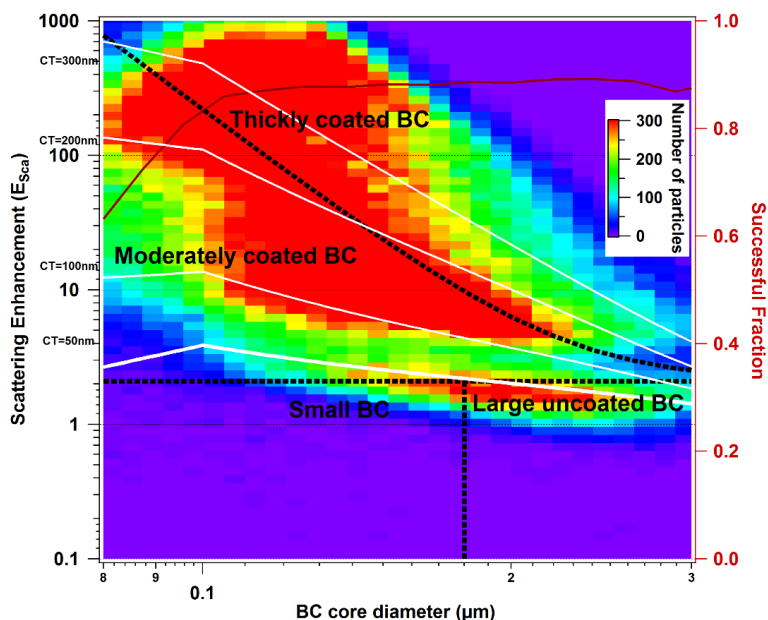
Figure 6. Scattering enhancement (E_sca) as a function of BC core size (D_c) for the typical outflow airmasses during the ICARB-2018.The plot is colored by particle number concentration. The solid brown line, with the corresponding scale on the right axis, shows the number fraction of BC particles that were successfully determined according to their scattering signal at each D_c size. The image plot is a two-dimensional histogram for the detected particles. The particles are separated as four groups using the borders (from top to bottom) at y = 3.38+0.000436*x^-5.7, y = 2.1, x = 0.18, as shown by dashed black lines on the figure (Liu et al., 2019). The solid white lines show the absolute coating thickness (ACT, nm) mapped on the E_sca- D_c plot.

The main features in the figure are:

(a) A reasonable amount of moderately coated BC particles having ACT ~50-100 nm with scattering enhancements in the range E_sca ~2-10 were seen, and also a signification proportion of moderately coated BC particles with large scattering enhancement (E_sca ~10-100), which increased with BC core sizes during the ICARB cruise. This highlighted the substantial contribution from a combination of mixed sources that co-emit BC and condensable material (Liu et al., 2014; 2019).

(b) Even the smaller sized BC cores (which possibly originate from fossil fuel emissions and transform to larger cores during the atmospheric transit) were also significantly coated with resultant scattering enhancement > 100 during the ICARB-2018, which highlights the extent of aging of BC particles in the continental outflow. Such faster aging of smaller cores is possible in the polluted air masses (Gong et al., 2016). Similarly, faster aging of large BC particles that generally originate from biomass burning sources results in moderate to thicker coating (Schwarz et al., 2008; Gong et al., 2016) and amplified scattering enhancement (Liu et al., 2019), which is also seen from Fig.6.

(c) Remarkably, a greater proportion of thickly coated particles with varying BC core diameters and a wide range (5-800) of scattering enhancement values were also observed, further highlighting a strong mixed source influence of the continental outflow.

The high proportion of thick coating on BC particles can result in significant changes in the optical properties of black carbon aerosols. As reported by Brooks et al. (2019) from the measurements over the IGP, a significant fraction of moderately coated

Atmospheric
Chemistry
and Physics
Discussions

Open Access

EGU

BC particles with increased scattering enhancement were found to have higher mass absorption coefficient values over the Indo Gangetic Plain. They attributed this to vigorous mixing between various sources due to the high amounts of secondary aerosol formation and photochemical aging across northern India. The present scenario, with a steady pollutant outflow containing contributions from diverse sources, is akin to it. Such alterations to the mixing state of BC can contribute to significant enhancement in the absorbing characteristics of BC aerosols over the marine regions as they underdo aging while transiting from upwind source regions in the west and east coasts of India, which may have noteworthy regional climate implications.

The large uncoated rBC particles (core diameters > 0.18 µm and thin coatings of ACT < 50 nm) with low scattering enhancements were also found during our measurements but in small quantities. This is consistent with the findings of Brooks et al. (2019), who reported insignificant amounts of such particles over the Indian region during the pre-monsoon and monsoon seasons. Liu et al. (2019) described that large uncoated rBC particles indicate coal-burning emissions and suggested that larger core BC particles with no or thin coatings display minimal E_{sca} values. This can be due to significant bias introduced by the sphericity assumption used in the Mie calculations, and possible difference in the refractive index of BC produced from coal-burning from the value assumed (~2.26 ± 1.26i) in the Mie calculations used to derive E_{sca}. However, this aspect cannot be addressed in the present study in the absence of measurements of BC morphology or source-dependent refractive index of rBC. As such, a more detailed in-situ analysis is necessary to address this.

3.4 Association between BC coating thickness and NR-PM1.0 chemical species

The information on the nature of the coating material along with the state of mixing of BC particles gives insight into the magnitude of the mixing-induced absorption enhancement for BC (Cappa et al., 2012, 2018; Peng et al., 2016; Liu et al., 2017). We have used the concurrent measurements of non-refractory PM1.0 (NR-PM1.0) aerosol mass and chemical composition data from the ACSM to infer the nature of coating material during the ICARB-2018. It may be noted that there is a possibility that BC is mixed externally with coarse mode aerosols like dust or sea-salt aerosols in the real atmosphere. But the synoptic circulation during the ICARB-2018 has not been favorable for significant dust transport to marine regions covered here. Also, prevailing wind speeds were too low for considerable in-situ production of sea salt aerosols. Therefore, the fraction of BC aerosols mixed with coarse mode particles is considered insignificant in our study.

General features of NR-PM1.0 chemical composition are shown in Fig.7, which shows the sub-regional mean mass concentrations and mass fractions (MF) of different species over the oceanic regions covered during the cruise.
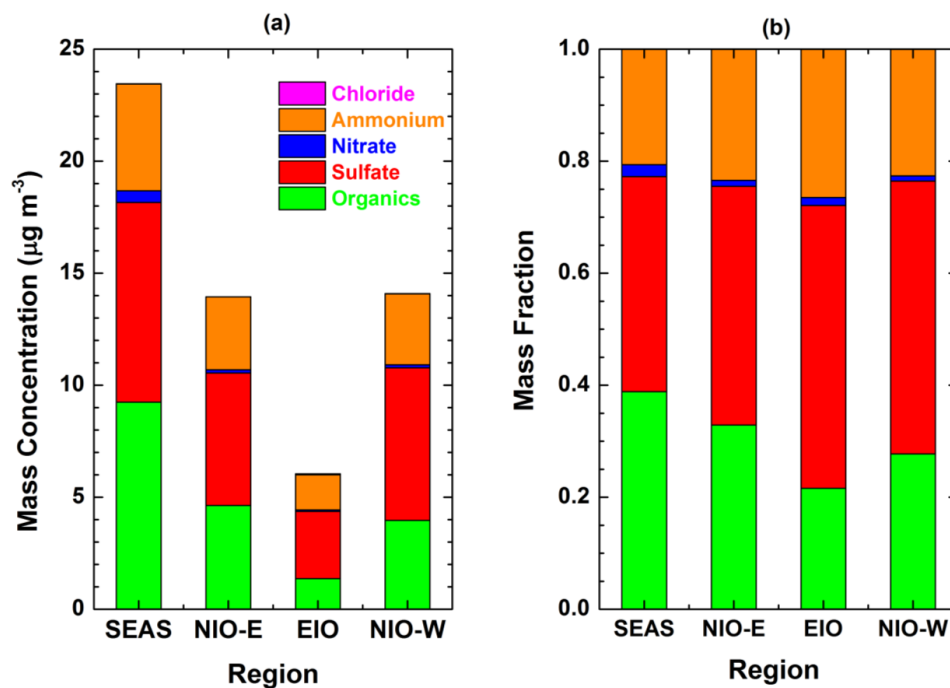
Figure 7. (a) Mass concentration and (b) mass fraction of NR-PM1.0 chemical species, organics, sulfate, ammonium, nitrate, and chloride over different sub-regions during the ICARB-2018.

In line with the pattern for rBC, the overall NR-PM1.0 aerosol mass concentration was also highest over the SEAS (mean
5   ~23.44 ± 5.07 µg m^{-3}), decreasing steadily further away from the continent to reach the lowest concentrations (~5.48 ± 2.83 µg m^{-3}) over the EIO, where mostly oceanic air masses prevailed. Sulfate and organics were the two major species dominating the NR-PM1.0 composition. Of these two, sulfate dominated most of the oceanic sub-regions with a mass- fraction ≥ 0.4 except for the SEAS region, where organics (~ 0.39) were also equally important. The mass-fraction of ammonium, which is formed through gas-phase and aqueous-phase chemical reactions of NH$_3$ produced from animal wastes, fertilizers, ocean, and soil, was
10   in the range ~0.20-0.23, while nitrate (0.01-0.02) and chloride are negligible in all the regions. To summarise, the South Asian outflow plumes consist of the organics-rich aerosol system in the vicinity of west coast/peninsular India, gradually changing to a sulfate-rich aerosol system in the remote oceanic regions. This marked change from the prominent presence of organics plus sulfate over coastal regions to a strong sulfate dominance over the remote oceanic regions emphasized the atmospheric processes (formation, transformation, and removal) at play in determining the lifecycle of these species during their transport.
15   Possible oxidation of primary particulate organic matter due to heterogeneous reactions involving oxidants such as OH, O$_3$, and NO$_3$ during long-range transport can result in their volatilization, restricting their lifetime. However, sulfate can be produced through the gas to particle conversion in the SO$_2$ rich air masses originated over the Indian region or through the dimethyl sulfide (DMS) pathway from the marine emissions. During long-range transport, in-situ oxidation of SO$_2$ by OH radicals in the gas phase followed by condensation onto pre-existing particles, or reaction of S(IV) via H$_2$O$_2$ and O$_3$ in the
20   aqueous phase can lead to enhanced sulfate concentrations. All such processes could have contributed to observed spatial heterogeneity in the observed organics to sulfate concentrations. Detailed investigation of these processes is not the scope of the present study.

        Further, the association between ammonium and sulfate (Fig. S3) was variable across the cruise. The mean molar ratios were ~1.44, 1.47, 1.43, and 1.25 mol/mol over the SEAS, the NIO-E, the EIO, and the NIO-W regions, respectively,

which indicated an NH_4^+ deficit (Aswini et al., 2020). The spatial variation of molar ratios of ammonium to sulfate is shown in the Supplement (Fig. S3, panel a). The association between submicrometre sulfate and ammonium mass concentrations depicted an excellent correlation (r>0.95) during the ICARB-2018 (Fig. S3b in the Supplement) with varying slopes indicating the extent of neutralization (higher molar ratios and an increased tendency towards neutralization of sulfate near the coastal

5   regions compared far away regions) of sulfate by ammonium. The present observation is consistent with those reported by Aswini et al. (2020), who suggested that *just-enough* ammonium was present to neutralize sulfate during the ICARB-2018 based on concurrent bulk aerosol chemistry using offline (filter paper sampling) technique. It is possible that when insufficient ammonium is present in the atmosphere, it can lead to the sulfate aerosols existing in forms other than $(NH_4)_2SO_4$. A probable reason for ammonium deficiency could be the difference in the lifetimes of gaseous ammonia and SO_2, which are precursors

10   for particulate sulfate and ammonium. Though dominant sources were located over the land for both the precursors, the sulfate aerosol can be formed from the oxidation of transported SO_2 over the ocean, whereas ammonia is lost rapidly away from the source regions. This is evident from the varying slopes seen in Fig. S3b.

We have examined the association between bulk absolute coating thickness (inferences did not change even we use RCT) and mass concentrations of NR-PM1.0 organic aerosols, sulfate, and ammonium during the campaign (Fig. 8) when

15   ACT is low (ACT < 50 % of MMD) (Fig.8, a-c) and high (ACT > 50% of MMD) (Fig. 8 d-f). The color bar indicates the values of the corresponding mass median diameters (MMD). The solid line is the linear least-squares fit between the variables, and the corresponding correlation coefficient (Pearson's r) is also shown in the figure.
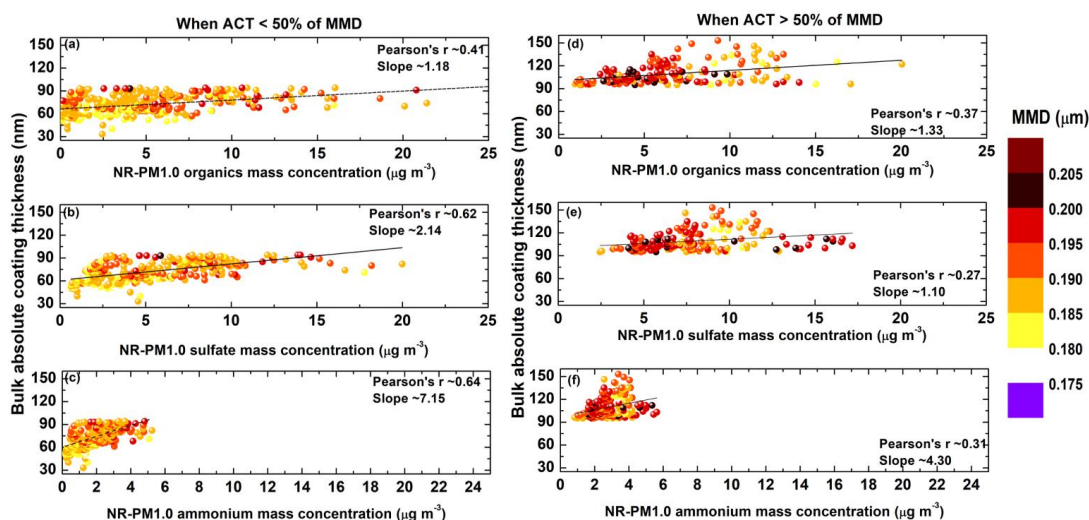

Figure 8. Scatter plot between the mass concentrations of non-refractory PM1.0 organics, sulfate, and ammonium
20   **aerosols and bulk absolute coating thickness during the ICARB-2018 for the observations with low ACT (a-c) and high ACT (d-f). Color represents the corresponding mass median diameter value. Solid lines represent the linear least-squares fit to the points. Regression slopes and correlation coefficients are written in each panel.**

Regression analysis suggested two distinct regression lines in the sulfate and ammonium plots. The bulk ACT showed a reasonable association (r > 0.6; p <0.01) with NR-PM1.0 sulfate and ammonium and a weaker association with organics (r

25   ~0.41; p <0.01) during low (ACT < 50% of MMD) observations. Corresponding slopes indicated that ACT on BC intensified more steeply with an enhanced mass concentration of sulfate (slope ~2.14) compared to organics (slope ~1.18), whereas the steepest enhancement in the ACT was noticed for ammonium (slope ~7.15). In contrast, there is no significant association between bulk ACT and mass concentrations of NR-PM1.0 species during high ACT (ACT > 50 % of MMD) observations. In this case, higher ACT values prevailed for all values of sulfate (or organics) and ammonium. The low and high ACT groups

of observations are distinctly separated by the corresponding MMDs values, where more frequent higher MMD values were seen for the BC population having a higher coating.

Thus, Fig. 8 suggested the possibility of complex coating on BC in the proximity of continental outflow where higher ACT (also higher MMD), significant amounts of organics, and ammonium were observed. In the far oceanic regions, sulfate components can act as a relatively dominant coating material on BC (compared to organics). This is not unexpected considering the aged BC particles present in the remote marine boundary layer dominated by the sulfate aerosol system. Previously, Ueda et al. (2018) reported morphological features of soot-containing particles over the Southern Ocean and suggested that aged soot-containing particles were transformed by soluble materials derived from dimethyl sulfide (DMS) oxidation during the summer. Though this DMS oxidation pathway may not be strong for in-situ production during the winter, it may be important when the reactions during entrainment of free tropospheric air masses into remote marine atmospheric boundary layer are considered (e.g., Clarke and Kapustin, 2002). Zhang et al. (2008) suggested that soot particles acquire a large mass-fraction of sulfuric acid during atmospheric aging. It is well known that semivolatile organic compounds are lost during aging due to evaporation following the dilution and oxidation of primary organics due to heterogeneous reactions (Donahue et al., 2006; Lambe et al., 2013). Such aging (the degree of oxygenation) of organics has previously been identified by increasing f_{44} and decreasing f_{43}, which are the ratios between the mass-to-charge ratios at 44 and 43 and the total organics signal in the component mass spectrum respectively (Ng. et al., 2011). During this cruise, gradual increases in f_{44} and decreases in f_{43} were observed with distance from the coast. However, as described earlier, sulfate concentrations can increase due to heterogeneous in-situ oxidation of SO_2 and condensation of sulfuric acid onto pre-existing particles after gas-phase oxidation of SO_2 during long-range transport (Kompalli et al., 2020a and references therein). These processes can alter the mixing state of BC, which is a relatively longer-lived species, and determine its dominant coating material. Another interesting possibility is organo-sulfates acting as a coating material on BC, but examining it is beyond the scope of the present study.

The MMD values of rBC showed no particular pattern with changing NR-PM1.0 species mass concentrations. Further, the rBC mass concentrations showed a good association with organics (r ~0.78) and sulfate (r ~0.71) (not shown), corroborating the presence of multiple sources which co-emit particulate organics and sulfate along with BC aerosols. All these suggested the presence of distinct sources and atmospheric processes involving a range of condensing gaseous species contributing to the BC coating, altering its mixing state by enhancing the extent of the coating. However, it is not possible to precisely demarcate the sources and coating substances at the individual particle level in this study. In-situ morphological analysis techniques (like transmission electron microscope (TEM) equipped with an energy dispersive X-ray analyzer) (Adachi et al., 2010, 2014; Ueda et al., 2016, 2018) are needed for identification of particle-level morphology.

The present study focused on the characterization of refractory BC microphysical properties, including its mixing state information for the first-time over the Southeastern Arabian Sea and the northern and equatorial Indian Ocean regions, which were influenced by distinct outflow air masses (that originated over the east coast/Bay of Bengal, the west coast/ peninsular India and marine regions) and traversed over the oceanic regions. The sensitivity of the optical, hygroscopic properties of BC to these observed characteristics and the estimation of regional radiative and climatic implications due to such highly aged, thickly coated large BC particles form the scope of future study.

4. Summary and Conclusions

In the present study, first-ever measurements of refractory BC microphysical properties (mass/number size distributions and mixing state parameters) over the oceanic regions adjacent to the Indian continent during periods of outflow have been carried out as part of the ICARB-2018. Major findings are the following:

(1) The rBC mass concentrations were highest over the coastal region of the Southeastern Arabian Sea (mean~938 ± 293 ng m^{-3}), which received continental outflow directly from the western coast/peninsular India and dropped to the

Atmospheric
Chemistry
and Physics
Discussions
Open Access
EGU

lowest concentrations over the remote EIO (206 ± 114 ng m^{-3}), where the impact of outflow was very weak. Nevertheless, the significant concentrations (mean > 500 ng m^{-3}) observed over the NIO region, distant from the sources, highlighted the transport efficiency of the rBC and the widespread nature of the continental outflow.

(2) BC size distributions indicated highly mixed BC sources, likely including a combination of fossil fuel and solid fuel sources, along with the restructuring of the cores of the aged BC particles. Despite widely varying magnitudes of the rBC mass loading, the mass median diameter (MMD) values were in a narrow range of 0.18-0.21 µm in all the regions due to the persistent outflow.

(3) Importantly, the continental outflow from the Indian region to the adjacent oceans is characterized by thickly coated BC particles, which may have significant regional climatic implications. A great degree of coating on rBC particles and large variability of mixing state parameters was found over the SEAS region (median RCT~ 2.15, ACT ~109 nm) that is greatly impacted by short-range continental outflow. The coating parameters showed a clear east-west contrast over the northern Indian Ocean with higher coatings and a narrow distribution over the NIO-E region (RCT ~ 2.05, ACT~104 nm) where east coast/ the Bay of Bengal air masses prevailed, compared to the NIO-W (RCT ~ 1.92, ACT~86 nm) that received west coast/peninsular India air masses. Observed lower coatings on rBC over the remote EIO (RCT~1.73, ACT~ 69 nm) suggested the possible role of preferential scavenging processes removing both internally mixed, large, thickly coated BC particles and potential condensable soluble material.

(4) The average fraction of rBC containing particles (F_{BC}) was in the range of 0.20-0.28 over different regions, which highlighted the presence of significant non-BC particles, more so over the coastal regions. Despite similar rBC core diameters (and the fraction of rBC containing particles) due to like sources, coated BC diameters varied according to the magnitude of the coating. The highest volume-weighted coated BC size ($D_{p,v}$) values were seen over the SEAS (mean ~ 0.41 ± 0.04 µm) and the NIO-1 (mean ~ 0.41 ± 0.01 µm), reflecting the vast extent of coating on BC in the air masses impacted by pollution outflow, compared to the EIO (0.33 ± 0.04 µm) which largely received marine air masses. Further, high values (4.5-18.3) of the bulk mixing ratio of coating mass to rBC mass ($M_{R,bulk}$) were noticed in the outflow regions due to the presence of such thickly coated BC particles. Substantial $M_{R,bulk}$ (~ 4.3 ± 1.52) values were found even over the EIO region, which may be associated with both emissions and atmospheric processes like aging.

(5) Examination of the size-resolved BC mixing state revealed, unlike the studies reported over urban regions, the absence of any notable small BC with a thin coating (MMD< 0.18 µm and ACT < 50 nm), typically associated with traffic emissions. A significant proportion of moderately coated BC particles (with bulk ACT ~50-100 nm) with two different ranges of scattering enhancement (E_{sca} ~ 2-10 and ~10-100) were noticed due to the mixed nature of BC sources (a combination of solid-fuel and fossil fuel emissions) in the outflow. Notably, a higher proportion of thickly coated particles (ACT >200 nm) with E_{sca} spanning over a wide range of 5-800 highlighted a distinct mixed source influence of the continental outflow from the Indian region to the surrounding oceanic regions.

(6) The non-refractory submicrometre aerosol chemical composition in the continental outflow is mostly dominated by sulfate, except for the coastal regions where organics were also found in significant quantities. The association between the non-refractory mass concentrations of particulate less than 1 µm in diameter (NR-PM1.0) and bulk absolute coating thickness of rBC was weak for high ACT observations (seen in the proximity of sources), suggesting complex coatings. In contrast, for the BC population with low ACT values observed over the remote ocean where sulfate was the dominant NR-PM1.0 species, a significant correlation (r ~0.62; p <0.01) was found between sulfate and rBC coating.

Atmospheric
Chemistry
and Physics
Discussions

Data availability

Data are available upon request from the contact author, S. Suresh Babu (s_sureshbabu@vssc.gov.in).

Competing interests

The authors declare that they have no conflict of interest.

5 **Author contributions**

SSB and SKK conceptualized the experiment and finalized the methodology. VSN, JV, SKK, MMG, and SSB were involved in the data collection onboard ship. SKK carried out the scientific analysis of the data supported by MF, DL. SKK drafted the manuscript. SSB, SKS, KKM, and HC carried out the review and editing of the manuscript.

References

Adachi, K., Zaizen, Y., Kajino, M. and Igarashi, Y.: Mixing state of regionally transported soot particles and the coating effect on their size and shape at a mountain site in Japan, J. Geophys. Res. Atmos., 119, 2014, 5386–5396,

25 doi:10.1002/2013JD020880.

Adachi, K., Chung, S. H., and Buseck, P. R.: Shapes of soot aerosol particles and implications for their effects on climate, J. Geophys. Res.-Atmos., 115, D15206, doi:10.1029/2009JD012868, 2010.

Asnani, G.C.: Tropical Meteorology, Vol.1, and Vol.2, Indian Institute of Tropical Meteorology, Pashan, Pune, 1012 pp, 1993.

Aswini A.R., Hegde P., Aryasree S., Girach I. A., and Nair P. R.: Continental outflow of anthropogenic aerosols over Arabian

30 Sea and Indian Ocean during wintertime: ICARB-2018 campaign, Sci. Total Environ., 712, 135214, doi:10.1016/j.scitotenv.2019.135214, 2020.

Babu, S.S., Manoj, M.R., Moorthy, K.K., Gogoi, M.M., Nair, V.S., Kompalli, S.K., Satheesh, S.K., Niranjan, K., Ramagopal, K., Bhuyan, P.K. and Singh, D.: Trends in aerosol optical depth over Indian region: Potential causes and impact indicators. J. Geophys. Res., 118, 11: 794-11,806, 2013.

35 Babu, S. S., Gogoi, M. M., Kumar, V. H. A., Nair, V. S., and Moorthy, K.K.: Radiative properties of Bay of Bengal aerosols: Spatial distinctiveness and source impacts, J. Geophys. Res., 117, D06213, doi:10.1029/2011JD017355, 2012.

Babu, S. S., Moorthy, K. K., Manchanda, R. K., Sinha, P. R., Satheesh, S. K., Vajja, D. P., Srinivasan, S., and Kumar, V. H. A.: Free tropospheric black carbon aerosol measurements using high altitude balloon: Do BC layers build their own homes up in the atmosphere? Geophys. Res. Lett., 38, L08,803, doi:10.1029/2011GL046654, 2011.

Bollasina, M., Nigam, S., and Lau, K.-M.: Absorbing Aerosols and Summer Monsoon Evolution over South Asia: An
5   Observational Portrayal, J. Climate, 21, 3221–3239, doi:10.1175/2007JCLI2094.1, 2008.

Boos, W. R. and Storelvmo, T.: Near-linear response of mean monsoon strength to a broad range of radiative forcings, P. Natl. Acad. Sci. USA, 113, 1510–1515, doi:10.1073/pnas.1517143113, 2016.

Bond, T. C., Doherty, S. J., Fahey, D. W., Forster, P. M., Berntsen, T., De Angelo, B. J., Flanner, M. G., Ghan, S., Karcher, B., Koch, D., Kinne, S., Kondo, Y., Quinn, P. K., Sarofim, M. C., Schultz, M. G., Schulz, M., Venkataraman, C., Zhang,
10   H., Zhang, S., Bellouin, N., Guttikunda, S. K., Hopke, P. K., Jacobson, M. Z., Kaiser, J. W., Klimont, Z., Lohmann, U., Schwarz, J. P., Shindell, D., Storelvmo, T., Warren, S. G., and Zender, C. S.: Bounding the role of black carbon in the climate system: A scientific assessment, J. Geophys. Res. Atmos., 118, 5380–5552, doi:10.1002/jgrd.50171, 2013.

Bond, T. C., and Bergstrom, R. W.: Light absorption by carbonaceous particles: An investigative review, Aerosol Sci. Tech., 40, 27–67, doi:10.1080/02786820500421521, 2006.

15   Brooks, J., Liu, D., Allan, J. D., Williams, P. I., Haywood, J., Highwood, E. J., Kompalli, S. K., Babu, S. S., Satheesh, S. K., Turner, A. G., and Coe, H.: Black carbon physical and optical properties across northern India during pre-monsoon and monsoon seasons, Atmos. Chem. Phys., 19, 13079–13096, https://doi.org/10.5194/acp-19-13079-2019, 2019.

Cappa, C. D., Onasch, T. B., Massoli, P., Worsnop, D. R., Bates, T. S., Cross, E. S., Davidovits, P., Hakala, J., Hayden, K. L., Jobson, B. T., Kolesar, K. R., Lack, D. A., Lerner, B. M., Li, S.-M., Mellon, D., Nuaaman, I., Olfert, J. S., Petäjä, T.,
20   Quinn, P. K., Song, C., Subramanian, R., Williams, E. J., and Zaveri, R. A.: Radiative Absorption Enhancements Due to the Mixing State of Atmospheric Black Carbon, Science, 337, 1078–1081, doi:10.1126/science.1223447, 2012.

Cappa, C. D., Zhang, X., Russell, L. M., Collier, S., Lee, A. K. Y., Chen, C.-L., et al. : Light absorption by ambient black and brown carbon and its dependence on black carbon coating state for two California, USA, cities in winter and summer, J. Geophys. Res. Atmos., 124, 1550‑1577. https://doi.org/10.1029/2018JD029501, 2019.

25   Cheng, Y., Li, S.-M., Gordon, M., and Liu, P.: Size distribution and coating thickness of black carbon from the Canadian oil sands operations. Atmos. Chem. Phys., 18, 2653–2667, 2018.

Clarke, A.D., and Kapustin, V.N.: A Pacific aerosol 953 survey: I. A decade of data on particle production, transport, evolution, and mixing in the troposphere. J. Atmos. Sci., 59, 363–82, 2002.

Donahue, N.M., Robinson, A.L., Stanier, C.O. and Pandis, S.N.: Coupled partitioning, dilution, and chemical aging of
30   semivolatile organics. Environ. Sci. Technol. 40, 2635–2643, 2006.

Das, P. K.: The Monsoons, 5th IMO Lecture, WMO Rep. 613, World Meteorol. Org., Geneva, 1986.

D'Errico, M., Cagnazzo, C., Fogli, P. G., Lau, W. K. M., von Hardenberg, J., Fierli, F., and Cherchi, A.: Indian monsoon and the elevated-heat-pump mechanism in a coupled aerosol climate model, J. Geophys. Res.-Atmos., 120, 8712–8723, doi:10.1002/2015JD023346, 2015.

35   Gao, R. S., Schwarz, J. P., Kelly, K. K., Fahey, D. W., Watts, L.A., Thompson, T. L., Spackman, J. R., Slowik, J. G., Cross, E.S., Han, J. H., Davidovits, P., Onasch, T. B., and Worsnop, D.R.: A novel method for estimating light-scattering properties of soot aerosols using a modified single-particle soot photometer, Aerosol Sci. Tech., 41, 125–135, 2007.

Gogoi, M.M., Rao C.T, Jayachandran V, Kompalli, S. K., Nair, V.S., Rama Gopal, K., Babu, S.S.: Spatial gradient of aerosol mass concentrations and size distributions over southeastern Arabian Sea and equatorial Indian Ocean during ICARB-
40   2018, Atmos. Environ., 213, 727-738, http://dx.doi.org/doi.org/10.1016/ j.atmosenv.2019.06.038, 2019.

Gong, X. D., Zhang, C., Chen, H., Nizkorodov, S. A., Chen, J. M., and Yang, X.: Size distribution and mixing state of black carbon particles during a heavy air pollution episode in Shanghai, Atmos. Chem. Phys., 16, 5399–5411, 2016.

Gustafsson, Ö., M. Krusa, Z. Zencak, R. J. Sheesley, L. Granat, E. Engstrom, P. S. Praveen, P.S. P. Rao, C. Leck, and Rodhe, H.: Brown clouds over south Asia: Biomass or fossil fuel combustion? Science, 323, 495-498, doi:10.1126/science.1164857, 2009.

Huang, X., Ding, A., Liu, L., Liu, Q., Ding, K., Niu, X., Nie, W., Xu, Z., Chi, X., Wang, M., Sun, J., Guo, W., and Fu, C.: Effects of aerosol-radiation interaction on precipitation during biomass burning season in East China, Atmos. Chem. Phys., 16, 10063–10082, https://doi.org/10.5194/acp-16-10063-2016, 2016.

Huang, X. F., Gao, R. S., Schwarz, J. P., He, L. Y., Fahey, D. W., Watts, L. A., McComiskey, A., Cooper, O. R., Sun, T. L., Zeng, L. W., Hu, M., and Zhang, Y. H.: Black carbon measurements in the Pearl River Delta region of China, J. Geophys. Res.-Atmos.,116, D12208, doi:10.1029/2010jd014933, 2011.

Huang, X. F., Sun, T. L., Zeng, L. W., Yu, G. H., and Luan, S. J.: Black carbon aerosol characterization in a coastal city in SouthChina using a single particle soot photometer, Atmos. Environ.,51, 21–28, doi:10.1016/j.atmosenv.2012.01.056, 2012.

IPCC, 2013: Climate Change., The Physical Science Basis. Contribution of Working Group I to the Fifth Assessment Report of the Intergovernmental Panel on Climate Change (Stocker, T.F., D. Qin, G.-K. Plattner, M. Tignor, S.K. Allen, J. Boschung, A. Nauels, Y. Xia, V. Bex and P.M. Midgley (eds.)). Cambridge University Press, Cambridge, United Kingdom and New York, NY, USA, 2013, 1535 pp.

Jacobson, M. Z.: Strong Radiative Heating Due to the Mixing State of Black Carbon in Atmospheric Aerosols. Nature, 409:695–697, 2001.

Kompalli, S. K., Babu, S.S., Satheesh, S. K., Moorthy, K.K., Das, T., Boopathy, R., Liu, D., Darbyshire, E., Allan, J.D., Brooks, J., Flynn, M.J., and Coe, H.: Seasonal contrast in size distributions and mixing state of black carbon and its association with PM1.0 chemical composition from the eastern coast of India, Atmos. Chem. Phys., 20, 3135–3149, 2020a, https://doi.org/10.5194/acp-20-3135-2020.

Kompalli, S. K., Nair, V.S., Jayachandran, V., Gogoi, M.M., and Babu, S.S.: Particle number size distributions and new particle formation events over the northern Indian Ocean during continental outflow, Atmos. Environ., 238, 117719, 2020b, https://doi.org/10.1016/j.atmosenv.2020.117719.

Kompalli, S.K., Moorthy, K.K., Babu, S.S.: Rapid response of atmospheric BC to anthropogenic sources: observational evidence, Atmos. Sci. Lett. 15, 166–171. http:// dx.doi.org/10.1002/asl2.483, 2014.

Kompalli, S.K., Babu, S.S., Moorthy, K.K., Gogoi, M.M., Nair, V.S., Chaubey, J.P.: Seasonal variation of aerosol black carbon distribution over the Bay of Bengal: multi-campaign measurements, Atmospheric Environment. 64, 366-373, DOI: 10.1016/ j.atmosenv.2012.09.073, 2013.

Kondo, Y., Matsui, H., Moteki, N., Sahu, L., Takegawa, N., Kajino, M., Zhao, Y., Cubison, M. J., Jimenez, J. L., Vay, S., Diskin, G. S., Anderson, B., Wisthaler, A., Mikoviny, T., Fuelberg, H. E., Blake, D. R., Huey, G., Weinheimer, A. J., Knapp, D. J., and Brune, W. H.: Emissions of black carbon, organic, and inorganic aerosols from biomass burning in North America and Asia in 2008, J. Geophys. Res., 116, D08204, doi:10.1029/2010JD015152, 2011.

Laborde, M., Crippa, M., Tritscher, T., Jurányi, Z., Decarlo, P. F., Temime-Roussel, B., Marchand, N., Eckhardt, S., Stohl, A., Baltensperger, U., Prévôt, A. S. H., Weingartner, E., and Gysel, M.: Black carbon physical properties and mixing state in the European megacity Paris, Atmos. Chem. Phys., 13, 5831–5856, 2013.

Laborde, M., Mertes, P., Zieger, P., Dommen, J., Baltensperger, U., and Gysel, M.: Sensitivity of the Single Particle Soot Photometer to different black carbon types, Atmos. Meas. Tech., 5, 1031–1043, doi:10.5194/amt-5-1031-2012, 2012.

Lambe, A. T., Cappa, C. D., Massoli, P., Onasch, T. B., Forestieri, S. D., Martin, A. T., Cummings, M. J., Croasdale, D. R., Brune, W. H., Worsnop, D. R., and Davidovits, P.: Relationship between oxidation level and optical properties of secondary organic aerosol, Environ. Sci. Technol., 47, 6349–6357, 2013.

Lawrence, M. G., and Lelieveld, J.: Atmospheric pollutant outflow from southern Asia: A review. Atmos. Chem. Phys., 10, 11,017 – 11,096, 2010.

Liu, D., Joshi, R., Wang, J., Yu, C., Allan, J. D., Coe, H., Flynn, M. J., Xie, C., Lee, J., Squires, F., Kotthaus, S., Grimmond, S., Ge, X., Sun, Y., and Fu, P.: Contrasting physical properties of black carbon in urban Beijing between winter and summer, Atmos. Chem. Phys., 19, 6749-6769, https://doi.org/10.5194/acp-19-6749-2019, 2019.

Liu, D., Whitehead, J., Alfarra, M. R., Reyes-Villegas, E., Spracklen, D. V., Reddington, C. L., Kong, S., Williams, P. I., Ting, Y.-C., Haslett, S., Taylor, J. W., Flynn, M. J., Morgan, W. T., McFiggans, G., Coe, H., and Allan, J. D.: Black-carbon absorption enhancement in the atmosphere determined by particle mixing state, Nat. Geosci., 10, 184–188, https://doi.org/10.1038/ngeo2901, 2017.

Liu, D., Taylor, J. W., Crosier, J., Marsden, N., Bower, K. N., Lloyd, G., Ryder, C. L., Brooke, J. K., Cotton, R., Marenco, F., Blyth, A., Cui, Z., Estelles, V., Gallagher, M., Coe, H., and Choularton, T. W.: Aircraft and ground measurements of dust aerosols over the west African coast in summer 2015 during ICE-D and AER-D, Atmos. Chem. Phys., 18, 3817–3838, https://doi.org/10.5194/acp-18-3817-2018, 2018.

Liu, S., Aiken, A. C., Gorkowski, K., Dubey, M. K., Cappa, C. D., Williams, L. R., Herndon, S. C., Massoli, P., Fortner, E. C., Chhabra, P. S., Brooks, W. A., Onasch, T. B., Jayne, J. T., Worsnop, D. R., China, S., Sharma, N., Mazzoleni, C., Xu, L., Ng, N. L., Liu, D., Allan, J. D., Lee, J. D., Fleming, Z. L., Mohr, C., Zotter, P., Szidat, S., and Prevot, A.S. H.: Enhanced light absorption by mixed source black and brown carbon particles in UK winter, Nat. Commun., 6, 8435;https://doi.org/10.1038/ncomms9435, 2015.

Liu, D., Whitehead, J., Alfarra, M. R., Reyes-Villegas, E., Spracklen, Dominick V., Reddington, Carly L., Kong, S., Williams, Paul I., Ting, Y.-C., Haslett, S., Taylor, Jonathan W., Flynn, Michael J., Morgan, William T., McFiggans, G., Coe, H., and Allan, James D.: Black-carbon absorption enhancement in the atmosphere determined by particle mixing state, Nat. Geosci., 10, 184-188, 10.1038/ngeo2901, 2017.

Liu, D., Allan, J. D., Young, D. E., Coe, H., Beddows, D., Fleming, Z. L., Flynn, M. J., Gallagher, M. W., Harrison, R. M., Lee, J., Prevot, A. S. H., Taylor, J. W., Yin, J., Williams, P. I., and Zotter, P.: Size distribution, mixing state and source apportionment of black carbon aerosol in London during wintertime, Atmos. Chem. Phys., 14, 10061–10084, https://doi.org/10.5194/acp-14- 10061-2014, 2014.

Liu, D., Allan, J., Whitehead, J., Young, D., Flynn, M., Coe, H., McFiggans, G., Fleming, Z. L., and Bandy, B.: Ambient black carbon particle hygroscopic properties controlled by mixing state and composition, Atmos. Chem. Phys., 13, 2015–2029, doi:10.5194/acp-13-2015-2013, 2013.

Liu, D., Flynn, M., Gysel, M., Targino, A., Crawford, I., Bower, K., Choularton, T., Jurányi, Z., Steinbacher, M., Hüglin, C., Curtius, J., Kampus, M., Petzold, A., Weingartner, E., Baltensperger, U., and Coe, H.: Single particle characterization of black carbon aerosols at a tropospheric alpine site in Switzerland, Atmos. Chem. Phys., 10, 7389–7407, doi:10.5194/acp-10-7389- 2010, 2010.

McMeeking, G. R., Morgan, W. T., Flynn, M., Highwood, E. J., Turnbull, K., Haywood, J., and Coe, H.: Black carbon aerosol mixing state, organic aerosols, and aerosol optical properties over the United Kingdom, Atmos. Chem. Phys., 11, 9037–9052, 2011.

McMeeking, G. R., Hamburger, T., Liu, D., Flynn, M., Morgan, W. T., Northway, M., Highwood, E. J., Krejci, R., Allan, J. D., Minikin, A., and Coe, H.: Black carbon measurements in the boundary layer over western and northern Europe, Atmos. Chem. Phys., 10, 9393–9414, 2010.

Meehl, G.A., Arblaster, J.M., and Collins, W.D., 2008. Effects of black carbon aerosols on the Indian monsoon. Journal of Climate, 21, 2869–2882.

Menon, S., Hansen, J., Nazarenko, L., and Luo, Y. F.: Climate effects of black carbon aerosols in China and India, Science, 297, 2250–2253, 2002.

Middlebrook, A. M., Bahreini, R., Jimenez, J. L., and Canagaratna, M. R.: Evaluation of Composition-Dependent Collection Efficiencies for the Aerodyne Aerosol Mass Spectrometer using Field Data, Aerosol Sci. Tech., 46, 258–271, doi:10.1080/02786826.2011.620041, 2012.

Miyakawa, T., Oshima, N., Taketani, F., Komazaki, Y., Yoshino, A., Takami, A., Kondo, Y., Kanaya, Y.: Alteration of the size distributions and mixing states of black carbon through transport in the boundary layer in east Asia, Atmos. Chem. Phys., 17, 5851–5864, 2017.

Moffet, R.C., and Prather, K.A.: In-situ measurements of the mixing state and optical properties of soot with implications for radiative forcing estimates, PNAS,106,11872–11877, 2009.

Moorthy, K.K.: South Asian aerosols in perspective: Preface to the special issue, Atmos. Environ, 125,307–311,2016, http://dx.doi.org/10.1016/j.atmosenv.2015.10.073.

Moorthy, K.K., Satheesh, S.K., Babu, S.S., and Dutt, C.B.S.: Integrated campaign for aerosols, gases, and radiation budget (ICARB): an overview, J. Earth Syst. Sci., 117 (S1), 243–262, 2008.

Moorthy, K. K., Sunilkumar, S.V., Pillai, P.S., Parameswaran, K., Nair, P.R., Ahmed, Y.N., Ramgopal, K., Narasimhulu, K., Reddy, R.R., Vinoj, V., Satheesh, S.K., Niranjan, K., Rao, B.M., Brahmanandam, P.S., Saha, A., Badarinath, K.V.S., Kiranchand, T.R., Latha, K.M.: Wintertime spatial characteristics of boundary layer aerosols over peninsular India, J. Geophys. Res., 110, D08207,doi:10.1029/2004JD005520, 2005.

Moteki, N. and Kondo, Y.: Effects of mixing state on black carbon measurements by laser-induced incandescence, Aerosol Sci. Technol., 41, 398–417, 2007.

Moteki, N. and Kondo, Y.: Dependence of laser-induced incandescence on physical properties of black carbon aerosols: Measurements and theoretical interpretation, Aerosol Sci. Tech., 44, 663-675, 2010.

Nair, V. S., Jayachandran, V. N., Kompalli, S.K., Gogoi, M. M., Babu, S. S.: Cloud condensation nuclei properties of South Asian outflow over the northern Indian Ocean during winter. Atmos. Chem. Phys., 20, 3135–3149, 2020, https://doi.org/10.5194/acp-20-3135-2020.

Ng, N. L., Herndon, S. C., Trimborn, A., Canagaratna, M. R., Croteau, P. L., Onasch, T. B., Sueper, D., Worsnop, D.R., Zhang, Q. , Sun, Y. L., Jayne, J. T.: An Aerosol Chemical Speciation Monitor (ACSM) for Routine Monitoring of the Composition and Mass Concentrations of Ambient Aerosol, Aero.Sci.Tech., 45:7, 780-794, 2011, doi:10.1080/02786826.2011.560211.

Pandey, A., Sadavarte, P., Rao, A. B., Venkataraman, C.: Trends in multi-pollutant emissions from a technology-linked inventory for India: II. Residential, agricultural and informal industry sectors. Atmos. Environ., 99, 341-352, 2014.

Peng, J., Hu, M., Guo, S., Du, Z., Zheng, J., Shang, D., Levy Zamora, M., Zeng, L., Shao, M., Wu, Y.-S., Zheng, J., Wang, Y., Glen, C. R., Collins, D. R., Molina, M. J., and Zhang, R.: Markedly enhanced absorption and direct radiative forcing of black carbon under polluted urban environments, P. Natl. Acad. Sci. USA, 113, 4266–4271, doi:10.1073/pnas.1602310113, 2016.

Ramanathan, V. and Carmichael, G.: Global and regional climate changes due to black carbon, Nat. Geosci., 1, 221–227, 2008.

Ramanathan, V., C. Chung, D. Kim, T. Bettge, L. Buja, J. T. Kiehl, W. M. Washington, Q. Fu, D. R. Sikka, and M. Wild: Atmospheric brown clouds: Impacts on South Asian climate and hydrological cycle, Proc. Natl. Acad. Sci. U.S.A., 102(15), 5326–5333, 2005.

Ramanathan, V., et al.: Indian Ocean Experiment: An integrated analysis of the climate forcing and effects of the great Indo-Asian haze, J. Geophys. Res., 106, 28,371- 28,398, 2001.

Raatikainen, T., Brus, D, Hooda1, R.K., Hyvärinen, A.P., Asmi, E., Sharma, V.P., Arola, A., Lihavainen, H., Size-selected black carbon mass distributions and mixing state in polluted and clean environments of northern India, Atmos. Chem. Phys., 17, 371-383, doi:10.5194/acp-17-371-2017, 2017.

Raatikainen, T., Brus, D., Hyvärinen, A.-P., Svensson, J., Asmi, E., and Lihavainen, H.: Black carbon concentrations and mixing state in the Finnish Arctic, Atmos. Chem. Phys., 15, 10057–10070, doi:10.5194/acp-15-10057-2015, 2015.

Reddington, C.L., McMeeking, G., Mann, G.W., Coe, H., Frontoso, M.G., Liu, D., Flynn, M., Spracklen, D.V., Carslaw, K.S.: The mass and number size distributions of black carbon aerosol over Europe. Atmos. Chem. Phys. 13, 4917–4939, 2013.

Sahu, L. K., Kondo, Y., Moteki, N., Takegawa, N., Zhao, Y., Cubison, M. J., Jimenez, J. L., Vay, S., Diskin, G.S., Wisthaler, A., Mikoviny, T., Huey, L. G., Weinheimer, A. J., and Knapp, D. J.: Emission characteristics of black carbon in anthropogenic and solid fuel burning plumes over California during ARCTAS-CARB 2008, J. Geophys. Res.,117, D16302, doi:10.1029/2011JD017401, 2012.

Schnaiter, M., Linke, C., Möhler, O., Naumann, K. H., Saathoff, H., Wagner, R., Schurath, U., and Wehner, B.: Absorption amplification of black carbon internally mixed with secondary organic aerosol, J. Geophys. Res., 110, D19204, https://doi.org/10.1029/ 2005JD006046, 2005.

Schwarz, J. P., Gao, R. S., Perring, A. E., Spackman, J. R., and Fahey, D. W.: Black carbon aerosol size in snow, Sci. Rep., 3, 1356, https://doi.org/10.1038/srep01356, 2013.

Schwarz, J. P., Gao, R. S., Spackman, J. R., Watts, L. A., Thomson, D. S., Fahey, D. W., Ryerson, T. B., Peischl, J., Holloway, J. S., Trainer, M., Frost, G. J., Baynard, T., Lack, D. A., de Gouw, J. A., Warneke, C., and Del Negro, L. A.: Measurement of the mixing state, mass, and optical size of individual black carbon particles in urban and biomass burning emissions, Geophys. Res. Lett., 35, L13810, doi:10.1029/2008GL033968, 2008.

Sedlacek, A. J., III, Lewis, E. R., Kleinman, L., Xu, J., and Zhang, Q. Determination of and evidence for noncore-shell structure of particles containing black carbon using the Single-Particle Soot Photometer (SP2), Geophys. Res. Lett., 39, L06802, 2012, doi:10.1029/2012GL050905.

Sedlacek, A. J., III, Onasch, T.B., Nichman, L., Lewis, E.R., Davidovits, P., Freedman, A., and Williams, L.: Formation of refractory black carbon by SP2-induced charring of organic aerosol, Aerosol Sci. and Technol., 52:12, 1345-1350, 2018, DOI:10.1080/02786826.2018.1531107.

Shiraiwa, M., Kondo, Y., Moteki, N., Takegawa, N., Miyazaki, Y., and Blake, D. R.: Evolution of mixing state of black carbon in polluted air from Tokyo, Geophys. Res. Lett., 34, L16803, https://doi.org/10.1029/2007GL029819, 2007.

Shiraiwa, M., Kondo, Y., Iwamoto, T., and Kita, K.: Amplification of light absorption of black carbon by organic coating, Aerosol Sci. Technol., 44, 46–54, 2010.

Srinivas, B., and Sarin, M.M.: PM2.5, EC and OC in atmospheric outflow from the Indo-Gangetic Plain: Temporal variability and aerosol organic carbon-to-organic mass conversion factor, Sci.of the Tot.Environ. 487,196–205,2014, http://dx.doi.org/10.1016/j.scitotenv.2014.04.002.

Srivastava, R. and Ramachandran, S.: The mixing state of aerosols over the Indo-Gangetic Plain and its impact on radiative forcing. Q. J. R. Meteorol. Soc. 139, 137–151. DOI:10.1002/qj.1958, 2013.

Taylor, J. W., Allan, J. D., Liu, D., Flynn, M., Weber, R., Zhang, X., Lefer, B.L., Grossberg, N., Flynn, J., Coe, H.: Assessment of the sensitivity of core/shell parameters derived using the single particle soot photometer to density and refractive index. Atmos. Meas. Tech. Discuss., 7,5491–5532, 2014.

Thamban, N.M., Tripathi, S.N., Shamjad P. M., Kuntamukkala, P., Kanawade, V.P.: Internally mixed black carbon in the Indo-Gangetic Plain and its effect on absorption enhancement. Atmos. Res., 197,211–223, http://dx.doi.org/10.1016/j.atmosres.2017.07.007, 2017.

Ueda, S., Osada, K., Hara, K., Yabuki, M., Hashihama, F., and Kanda, J.: Morphological features and mixing states of soot-containing particles in the marine boundary layer over the Indian and Southern oceans, Atmos. Chem. Phys., 18, 9207–9224, https://doi.org/10.5194/acp-18-9207-2018, 2018.

Ueda, S., Nakayama, T., Taketani, F., Adachi, K., Matsuki, A., Iwamoto, Y., Sadanaga, Y., and Matsumi, Y.: Light absorption and morphological properties of soot-containing aerosols observed at an East Asian outflow site, Noto Peninsula, Japan. Atmos. Chem. Phys., 16, 2525–2541, 2016.

Wang, J., Liu, D., Ge, X., Wu, Y., Shen, F., Chen, M., Zhao, J., Xie, C., Wang, Q., Xu, W., Zhang, J., Hu, J., Allan, J., Joshi, R., Fu, P., Coe, H., Sun, Y.: Characterization of black carbon-containing fine particles in Beijing during wintertime. Atmos. Chem.Phys. 19, 447‑458, 2019.

Wang, Q. Y., Cao, J., Han, Y., Tian, J., Zhu, C., Zhang, Y., Zhang, N., Shen, Z., Ni, H., Zhao, S., and Wu., J.: Sources and physicochemical characteristics of black carbon aerosol from the southeastern Tibetan Plateau: internal mixing enhances light absorption. Atmos. Chem. Phys., 18, 4639–4656, 2018.

Zhang, R., Khalizov, A.F., Pagels, J., Zhang, D., Xue, H., McMurry, P.H.: Variability in morphology, hygroscopicity, and optical properties of soot aerosols during atmospheric processing, PNAS, 105 (30) 10291-10296; DOI: 10.1073/pnas.0804860105, 2008.

Zhang, J., Liu, J., Tao, S., and Ban-Weiss, G. A.: Long-range transport of black carbon to the Pacific Ocean and its dependence on aging timescale, Atmos. Chem. Phys., 15, 11521–11535, https://doi.org/10.5194/acp-15-11521-2015, 2015.

Table A1. Symbols and abbreviations

Symbols/abbreviations	Meaning
ACSM	Aerosol chemical speciation monitor
ACT	Absolute coating thickness
D_c	BC core diameter
$D_{p,v}$	Volume-weighted coated BC size
E_{sca}	Scattering enhancement
EIO	Equatorial Indian Ocean
F_{BC}	Fraction of rBC containing particles
ICARB	Integrated Campaign for Aerosols, gases, and Radiation Budget
IGP	Indo Gangetic Plain
MMD	Mass median diameter
MSD	Mass size distribution
$M_{R,bulk}$	Bulk mixing ratio of coating mass over rBC mass
NIO	Northern Indian Ocean
NIO-E	Northern Indian Ocean eastern leg
NIO-W	Northern Indian Ocean western leg
NMD	Number median diameter
NR-PM1.0	Non-refractory PM1.0
SAS	Southern Arabian Sea
SEAS	Southeastern Arabian Sea
SP2	Single particle soot photometer
rBC	Refractory black carbon
RCT	Relative coating thickness